Numerical simulations of a sphere settling through a suspension of neutrally buoyant fibres

By OLIVER G. HARLEN[1], R. R. SUNDARARAJAKUMAR[2]
AND DONALD L. KOCH[2]

[1]Department of Applied Mathematics, University of Leeds, Leeds, LS2 9JT, UK

[2] School of Chemical Engineering, Cornell University, Ithaca, NY 14853, USA

The sedimentation of a small dense sphere through a suspension of neutrally buoyant fibres is investigated via a numerical simulation technique that includes both fibre–fibre contact forces and long-range hydrodynamic interactions. In situations where the diameter of the sphere is smaller than the length of the fibres, calculations that exclude the effect of contacts between fibres severely underestimate the drag force on the sphere measured in experiments. By including fibre–fibre contacts in our simulations we are to able to account for this discrepancy, and also the strong dependence of the drag on the initial orientation of the fibres. At low and moderate values of nL^3, where n is the number of fibres per unit volume and L the fibre length, hydrodynamic interactions are found to be important in moderating the effect of contacts between fibres.

An asymptotic solution is presented for the limit when the sphere diameter is much smaller than both the fibre length and inter-fibre spacing, but large compared to the fibre thickness. This is found to be in good agreement with the simulations.

Results of calculations on sedimentation through a monolayer of fibres are also presented, as a model of a semi-concentrated suspension. Collisions between fibres are much more frequent, due to the geometric confinement.

1. Introduction

Milliken *et al.* (1989) and Powell, Morrison & Milliken (1998) conducted a series of experiments in which they measured the sedimentation speed of a small dense sphere falling through a suspension of neutrally buoyant fibres in a viscous Newtonian fluid. The suspension was stirred before each experiment to randomize the initial orientation distribution of the fibres. Unlike a classical falling-ball experiment in which the sphere diameter is large compared to the length scale of the suspension microstructure, in these experiments the diameter of the spheres was smaller than the length of the fibres. Thus the normal assumptions made in analysing falling ball experiments, that the suspension can be viewed as a continuum on the length scale of the sphere and the velocity disturbance caused by the sphere is linear on the length scale of the fibres, are not valid for this experiment. It may also be noted that, even if the fibres were small compared to the ball diameter, a continuum description of the suspension would lead to an anisotropic viscosity that would be coupled with the flow-induced fibre orientation.
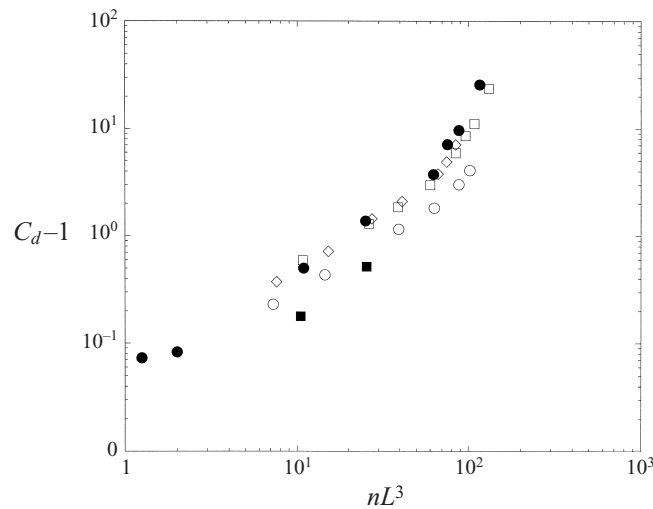
FIGURE 1. Plot of experimental measurements of the drag coefficient on a sphere falling through suspensions of initially randomly oriented fibres as a function of nL^3 for various fibre aspect ratios: •, $L/d = 19.8$ (from Milliken *et al*); □, $L/d = 30.7$; ○, $L/d = 47.8$; ◇, $L/d = 48.9$ (from Powell *et al*). Also plotted, as filled squares (■), are results for an initially vertically aligned suspension obtained by Mondy *et al.* (1990).

The combined data from both Milliken *et al.* and Powell *et al.* are plotted in figure 1 as the fractional increase in the drag coefficient on the sphere versus nL^3 where L is the fibre length and n is the number of fibres per unit volume. The fact that the results for different aspect ratios superpose demonstrates that nL^3 is the appropriate measure of fibre concentration here. Below a value of nL^3 of about 50, the additional drag increases approximately linearly with nL^3 as 0.04–$0.05nL^3$. For fibres of aspect ratio 20 this is more than a factor four larger than the increase in viscosity of a dilute suspension of randomly oriented fibres,

$$\frac{\mu - \mu_s}{\mu_s} = \frac{\pi nL^3}{90 \log(2r)} = 0.009nL^3,$$

where μ and μ_s are the viscosity of the suspension and the suspending fluid respectively. At concentrations above nL^3 of 50 the increase in drag becomes nonlinear, with the extra drag increasing approximately as $(nL^3)^3$. A further set of experiments were performed by Mondy *et al.* (1990) (filled square symbols in figure 1) using fibres which had a similar aspect ratio to those of Milliken *et al.*, but were initially aligned approximately vertically, rather than being randomly oriented. The additional drag coefficient was found to be much smaller, by about a factor of three, than that found for an initially randomly oriented suspension. This result contrasts with recent experiments by Ralambotiana, Blanc & Chaouche (1997) with spheres of 5 to 10 fibre lengths in diameter, who found the drag was indepedent of fibre orientation.

Rosenberg, Denn & Keunings (1990) performed numerical calculations of the falling-ball experiment. These calculations assume that the sphere diameter is large compared to the length of the fibres, so that the suspension may be treated as a continuum. The suspension itself is modelled using dilute theory, so that interactions between the fibres are neglected. The additional drag coefficient for ellipsoidal fibres of aspect ratio 20 was found to be $0.013nL^3$, an increase of approximately 40% on the viscosity of a dilute randomly oriented suspension. This demonstrates that

the flow-induced alignment of the fibres produces a small increase in the effective viscosity.

Rosenberg *et al.*'s calculations also found no appreciable difference in the drag coefficient between vertical and random initial fibre orientations, in line with the experiments of Ralambotiana *et al.* on large spheres. This suggests that the difference between the aligned and random suspensions found by Milliken *et al.* and Mondy *et al.* is a consequence of the small size of the sphere relative to the fibre length used in their experiments.

In addition to the flow-induced fibre alignment, another factor that produces an increase in drag is the effect of hydrodynamic interactions among the fibres. These were not included in Rosenberg *et al.*'s calculations. Hydrodynamic interactions are included in the Stokesian dynamics calculations for spheroids by Claeys & Brady (1993*b*) and Mackaplow & Shaqfeh's (1996) slender-body simulations. Both sets of calculations are static, in the sense that they use Monte-Carlo techniques to generate the configurations. The results from these two different techniques are in good agreement with each other and with the experiments of Bibbo (1987) on start-up of shear flow for values of nL^3 up to 30 for fibres of aspect ratio 50. At higher concentrations Mackaplow & Shaqfeh's results give a slightly higher increase in drag in line with Bibbo's results. For particles of aspect ratio 20, Claeys & Brady report that the additional viscosity varies linearly with nL^3, as approximately $0.017nL^3$ up to nL^3 of 30. This is an increase of approximately 80% on the viscosity of a dilute suspension but is again too small to explain the increase in drag coefficient measured by Milliken *et al.*

Adding together the increases in drag due to both flow-induced alignment and hydrodynamic interactions still gives an additional drag coefficient that is too small by factor of two. This suggests that there must be an additional mechanism at work in the experiments that is not included in these theories. In addition there is the question of why the drag coefficient in the experiments is so much higher for random initial orientation compared to vertical alignment, whereas the simulations suggest it should be approximately the same. A possible explanation for these discrepancies is the effect of collisions both between the fibres and between the ball and the fibres caused by the nonlinearity of the flow on the length scale of the fibres. In particular we would expect to see more collisions if the fibres are randomly oriented than if they are all vertical initially.

In linear flows, the fibres rotate along the trajectories of fluid line elements. As lines of fluid do not cross one another, the fibres will not come into close contact with one another until the number density of fibres, n, is of order $1/L^2 d$ (Sundararajakumar & Koch 1997), i.e. until the concentration of discs swept out by the rotating fibres exceeds unity. The velocity disturbance caused by the fibres decays on a length scale of order L, so that in a linear flow there is a range of concentrations ($1/L^3 \ll n \ll 1/(L^2 d)$), called *semi-dilute* where the fibres interact with one another via the fluid, but do not collide. However, if the flow is nonlinear, as in the case of the falling-sphere experiment, the fluid line elements will bend and so a rigid fibre cannot follow the trajectory of a fluid line element. Consequently collisions between fibres will occur at much lower fibre concentrations, as soon as n exceeds $1/L^3$, so that both long- and short-range interactions become important at the same order of concentration.

Much recent theoretical work has concentrated on predicting the effect of long-range interactions between fibres, mediated by the solvent, in semi-dilute suspensions where collisions between fibres can be neglected. This has provided results for the thermal, electrical, mechanical and rheological properties of a suspension (Batchelor

1971; Cates & Edwards 1984; Shaqfeh 1988; Fredrickson & Shaqfeh 1989; Shaqfeh & Fredrickson 1990) and predictions of the fibre orientation distribution (Koch & Shaqfeh 1990; Rahnama, Koch & Shaqfeh 1995).

In comparison, relatively little is known about the effect of collisions. In a suspension of Brownian fibres, where the fibres move independently of one another, the steric hindrance caused by collisions with neighbouring fibres greatly inhibits the diffusion of a fibre through the suspension (Doi & Edwards 1986). Toll & Manson (1994) derive an expression for the stress in a non-Brownian suspension on the assumptions that: the fibres are packed in parallel planes; the flow is in the plane of the fibre orientations; and the only force between fibres is sliding friction between fibres in neighbouring layers. Fibres in the same layer are assumed not to contact one another. Sandstrom & Tucker (1993) use a similar model to derive an effective rotary diffusivity for the fibres. It is clear that these studies take a phenomenological approach to model the effect of mechanical contacts, and are thus unable to provide a detailed understanding of the effect of mechanical contacts on the microstructure of the suspension.

In suspensions of smooth, spherical particles, lubrication forces are sufficiently strong to prevent mechanical contacts among the particles, thereby preserving the Stokes flow reversibility. However, the lubrication forces between fibres are much weaker, and one might expect the breakdown of lubrication, leading to mechanical contacts. Russel *et al.* (1971) and Stover & Cohen (1990) have observed the breakdown of Stokes flow reversibility in the case of fibres close to a solid boundary. This strongly suggests the possibility of mechanical contacts in fibre suspensions. In fact, we shall later show that the dominant short-range forces are due to direct contacts and that lubrication can be neglected. Longer range hydrodynamic interactions, over distances of the order of the fibre length, are important as they affect the frequency and severity of collisions.

In order to investigate the role of fibre contacts in the falling-ball experiment we have conducted some numerical simulations of a sphere falling through a suspension of neutrally buoyant fibres. A number of different techniques have been used for simulating suspensions of spheres, including Stokesian dynamics (Brady & Bossis 1988), the lattice Boltzmann technique (Ladd 1989), finite volume methods (Yuan & Ball 1994), and fast multi-pole methods (Sangani & Mo 1996). There have been relatively few simulations of suspensions of non-spherical particles. Mondy, Inger & Dingham (1991) used a boundary integral method to perform static calculations of a sphere surrounded by 24 rods. Claeys & Brady (1993*a*) developed a version of Stokesian dynamics for spheroidal fibres in which the multi-body hydrodynamic interactions are approximated as a force, torque and couple on each fibre, together with a more accurate representation of the two-body interaction to account for lubrication forces. In the simulations of Mackaplow & Shaqfeh (1996), the fibres are represented as line distributions of forces. This gives a more accurate representation of the multi-body interactions, but at the expense of greater computational cost. None of these methods includes mechanical contacts and past simulations have been restricted to either Monte-Carlo calculations, where the trajectories of the fibres are not followed in time, or to modest values of nL^3.

The simulations presented here differ from those described above in that they include mechanical contacts between fibres to prevent fibres from passing through one another. In determining fibre contacts the fibres are taken to be infinitely thin, so that the simulations correspond to the semi-dilute regime where $nL^2d \ll 1$ and contacts arise from nonlinearities in the flow. In order to be able to capture structures within the

suspension of several fibre lengths in size, one must calculate the motion of several thousand fibres simultaneously. In order to make the calculation computationally feasible it is necessary to approximate the hydrodynamic interactions.

Mackaplow & Shaqfeh showed that for fibre aspect ratios up to 20 the Stokesian dynamics method of Claeys & Brady provides a reasonably good approximation of the hydrodynamic interactions. The results from the two methods remain in good agreement for aspect ratio 50 particles up to nL^3 of 30. As our calculations with hydrodynamic interactions are restricted to this range of concentrations, we have chosen to use a method similar to Claeys & Brady, with a force, torque and stresslet on each fibre. However rather than placing point forces and dipoles at the centre of each fibre we distribute the forces along the entire length of fibre in order to improve accuracy at higher aspect ratios. This simplification allows us to simulate the motion of up to ten thousand fibres simultaneously.

In the next section we describe the method of simulation. Results for the drag coefficient for a sphere of diameter $0.5L$ are presented in §3, together with a comparison with the experimental results of Milliken *et al.* and Powell *et al.*. In §4, we consider how the drag coefficient varies with the diameter of the sphere and give an analytical expression for the limit when the ball diameter is small compared to the fibre length, but large compared to the fibre diameter. The fluctuations to the mean sedimentation speed of the sphere are considered in §5, where we compute the effective diffusivity of the sphere. Section 6 considers the effect of introducing friction between the fibres. Finally in §7 we consider the motion of a sphere falling through a monolayer of fibres, whose position and orientation are confined to a plane. In two dimensions fibre concentrations in the range $1 \ll nL^2 \ll L/d$ are *semi-concentrated*, and so provide a model of a three-dimensional semi-concentrated suspension.

2. Method of simulation

In order to simulate the experiment of Milliken *et al.*, we compute the path of a small dense sphere as it falls through a column of neutrally buoyant fibres. The initial positions and orientations of the fibres are assigned at random, and we follow the position and orientation of each fibre as the sphere falls. As in the experiment, we calculate the drag coefficient on the sphere from its average vertical speed during its descent averaged over either 25 or 10 different initial fibre configurations.

The motion of the sphere disturbs the fibres in two distinct ways. First, the sphere creates a disturbance in the fluid, which causes the fibres to translate and rotate. This fluid velocity is affected by the presence of all the other fibres in the suspension, and so the calculation of this long-range hydrodynamic interaction is a many-body problem involving all of the fibres. Second, if a fibre blocks the path of the sphere, the sphere and fibre will make direct contact with one another and there will be an equal and opposite reaction force acting on each body preventing interpenetration. Similarly, if two fibres try to cross one another, a reaction force prevents one fibre from passing through the other. These short-range contact forces act as constraints on the relative motion of the two contacting particles. The fibres will in turn affect the motion of the sphere, through both mechanical contacts and hydrodynamic disturbances mediated by the fluid.

These two types of disturbances are very different in character, and consequently are dealt with in different ways in the simulations. The long-range hydrodynamic interactions are represented via a fluid velocity, while the short-range interactions are represented as forces acting on the particles.

2.1. *Motion of the particles*

Using Faxén's law the velocity of the sphere $\dot{x}^{\text{sph}}$ may be written as

$$\dot{x}^{\text{sph}} = \left(1 + \frac{\sigma^2}{24}\nabla^2\right)\mathbf{u} + \frac{1}{3\pi\sigma}\left(\mathbf{W} + \sum_k \mathbf{N}_k\right), \tag{2.1}$$

where $\mathbf{u}$ is the sum of the velocity disturbances caused by the fibres and $\mathbf{N}_k$ are the forces caused by direct contacts with fibres. Here, σ is the sphere diameter, $\mathbf{W}$ is the net force of gravity on the ball. For convenience, we have divided all forces by the fluid viscosity. For friction-free contacts there are no couples acting on the sphere so that we do not need to calculate the angular velocity of the sphere.

The position and orientation of each fibre in the suspension can be described uniquely by the position vector of the centre of mass $\mathbf{x}$, and a unit vector $\mathbf{p}$ parallel to the major axis of the fibre. For a fibre with a high length to thickness ratio, the translational and rotational mobilities can be obtained from slender-body theory (Batchelor 1970). The translational and angular velocities, $\dot{x}$ and $\dot{p}$ respectively, of a fibre in a velocity field $\mathbf{u}$, subject to point forces $\mathbf{N}_k$ at positions $\mathbf{x} + \lambda^k \mathbf{p}$ along its length are given by

$$\dot{x} = \frac{1}{L}\int_{-L/2}^{L/2} \mathbf{u}(\mathbf{x} + s\mathbf{p})\mathrm{d}s + \frac{\log(2r)}{4\pi L}(\mathbf{I} + \mathbf{p}\mathbf{p})\cdot\sum_k \mathbf{N}_k, \tag{2.2}$$

$$\dot{p} = \frac{12}{L^3}(\mathbf{I} - \mathbf{p}\mathbf{p})\cdot\int_{-L/2}^{L/2} s\mathbf{u}(\mathbf{x} + s\mathbf{p})\mathrm{d}s + \frac{3\log(2r)}{\pi L^3}\sum_k \lambda^k \mathbf{N}_k\cdot(\mathbf{I} - \mathbf{p}\mathbf{p}). \tag{2.3}$$

Thus the evolution of the suspension microstructure may be calculated by integrating equations (2.1)–(2.3) once the contact forces $\mathbf{N}_k$ and fluid velocity $\mathbf{u}$ have been found. The calculation of $\mathbf{N}_k$ and $\mathbf{u}$ is described in the next two subsections.

2.2. *Short-range interactions – contact forces*

As noted above short-range interactions are treated as direct forces acting on the particles. Such interactions may include direct mechanical contacts between fibres, lubrication forces and colloidal forces. The fibres used in the experiments of Milliken *et al.* are large, approximately 3 cm in length, and so colloidal and Brownian forces are negligible.

For low-aspect-ratio particles such as smooth spheres, lubrication forces are sufficiently strong to prevent particles touching one another, and it might be thought that the same should be true of fibres. However, the lubrication force between high-aspect-ratio particles is much weaker.

The lubrication force between two spheres converging at speed U is equal to $3\pi U\sigma^2/4h$, where h is the shortest distance between the spheres. Thus, if the same force is applied to an isolated sphere, the sphere will move one radial distance in the time taken for the gap h to reduce by a factor of e^{-2}. Therefore, in the time taken for one sphere to roll around the other, the gap thickness will only reduce by one order of magnitude, and so the spheres will not touch. In contrast the lubrication force between a sphere of diameter σ and a fibre of length L and diameter d (where $d \ll \sigma \ll L$) is

$$\frac{3\pi U\sigma^{1/2}d^{3/2}}{h},$$

so that in the same time the gap will reduce by a factor of $\exp\left[-\frac{1}{2}(\sigma/d)^{3/2}\right]$

$(= 10^{-7}$ for $\sigma/d = 10)$. Therefore in a practical situation the gap will shrink below the roughness scale on the fibre. Even for perfectly smooth fibres this separation is so small that the continuum hypothesis is no longer valid. The lubrication force between two fibres is even weaker, and so we conclude that when particles come close to one another they make mechanical contact. Experiments by Stover & Cohen (1990) and Russel *et al.* (1971) show that close interactions between a fibre and a rigid wall do not obey Stokes' flow reversibility, so that non-hydrodynamic forces are involved. Furthermore, including the lubrication force delays the collision between the sphere and the fibre by a small time

$$\frac{3\pi\sigma d}{|\boldsymbol{W}|} \left(\frac{d}{\sigma}\right)^{3/2} \log\left(\frac{d}{l_r}\right)$$

where l_r is the roughness length. For a roughness length of $10^{-3}d$ and σ/d equal to 10 this corresponds to the time for an isolated sphere to fall a distance of 0.04 diameters and may be regarded as negligible. Thus we may neglect the effects of lubrication forces entirely, so that the only forces acting between the particles are rigid body contacts. Of course, this scaling argument only applies to the case when σ/d is large. If the sphere diameter is as small as the fibre diameter then lubrication forces between the sphere and the fibres are large, though the lubrication forces between fibres may still be neglected.

A new contact is created whenever two fibres that are not already in contact would have passed through one another. The problem of constructing an efficient algorithm to determine which pair of fibres in a suspension will be the first to intersect has been studied by Frenkel & Maguire (1983) in the context of molecular dynamics. The difference between molecular dynamics and our simulations is that we impose a maximum timestep Δt_0 after which the velocities and angular velocities of the fibres will be updated even though no new contacts occurred. The algorithm we use for detecting new contacts is similar to that of Frenkel & Maguire and contains the following three steps:

(*a*) Determine whether the fibre centres are ever less than L apart during the time interval. If they are not the fibres cannot have crossed one another. This is a very quick test to implement and eliminates a large number of possible pairs.

(*b*) Determine whether the lines through the fibres intersect. For this to happen there must be a time $t + \tau$, $(\tau \leqslant \Delta t)$ at which

$$(\boldsymbol{x}_\alpha - \boldsymbol{x}_\beta) \cdot (\boldsymbol{p}_\alpha \wedge \boldsymbol{p}_\beta) = 0.$$

(*c*) Finally, if the lines intersect the fibres will intersect provided that the contact point lies in the section of both lines within $L/2$ of the fibre midpoint.

Whenever a contact is detected the timestep Δt is reduced to the time when this contact formed. We also record the 'sign' of the contact by noting whether $(\boldsymbol{x}_\alpha - \boldsymbol{x}_\beta) \cdot (\boldsymbol{p}_\alpha \wedge \boldsymbol{p}_\beta)$ was positive or negative prior to the contact. The accuracy of our implementation of this algorithm was checked by performing molecular dynamic simulations for the same system studied by Frenkel & Maguire.

When two fibres are in contact there is a normal reaction force perpendicular to both fibres that prevents the fibres from crossing one another (see figure 2). The magnitude of this force is determined by the constraint that

$$\frac{\mathrm{d}}{\mathrm{d}t}\left[(\boldsymbol{x}_\alpha - \boldsymbol{x}_\beta) \cdot (\boldsymbol{p}_\alpha \wedge \boldsymbol{p}_\beta)\right] = 0. \tag{2.4}$$

The direction of the contact force on fibre α is defined to be $\boldsymbol{p}_\alpha \wedge \boldsymbol{p}_\beta$ multiplied by the
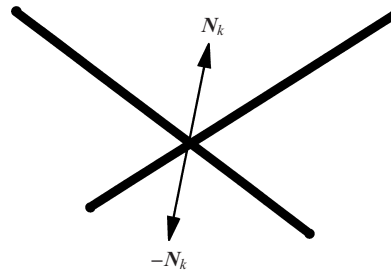
FIGURE 2. Sketch showing the direction of the reaction force N_k between two contacting fibres.

sign of the contact, so that the magnitude is positive for a repulsive force. In addition to the reaction force there may be a friction force that resists the sliding of one fibre across another. In the interests of simplicity we have taken the friction force to be zero in most of our simulations, but in §7 we discuss the changes that occur when a simple Coulomb friction law is applied between contacting fibres.

An existing contact between two fibres may break in one of two ways. One fibre may slide off the end of the other, or the reaction force may become negative, i.e. changing from a repulsive to an attractive force. The constraint force only acts to prevent interpenetration of fibres so that, on the assumption that there are no adhesive colloidal forces, there should be no resistance to the fibres lifting off one another. If a contact force is found to be negative (i.e. it is holding the fibres together rather than keeping them apart), then this contact is removed and the velocities and angular velocities of all the fibres are recalculated. A contact is broken by sliding when the contact point of one of the fibres reaches the end of the fibre, $\lambda^k = \pm L/2$.

2.3. Hydrodynamic interactions

Although lubrication forces between pairs of particles may be neglected, longer range hydrodynamic interactions over distances of the order of a fibre length L must be considered. These interactions are weak in comparison to short-range collisions, but they occur more frequently and may have important bearing on the frequency of collisions.

An isolated sphere at position x^{sph} and subject to a force F creates a velocity disturbance around it of the form

$$u^{\mathrm{sph}}(x) = H(x - x^{\mathrm{sph}}) \cdot F$$

where

$$H(x') = \frac{I}{24\pi a} \left\{ 3\left(\frac{a}{r}\right) + \left(\frac{a}{r}\right)^3 \right\} + \frac{x'x'}{8\pi a r^2} \left\{ \left(\frac{a}{r}\right) - \left(\frac{a}{r}\right)^3 \right\}. \tag{2.5}$$

Here I is the unit tensor, a ($= 0.5\sigma$) the sphere radius, and $r = |x'|$. In a suspension this disturbance is modified by the presence of fibres close to the sphere, so that the calculation of the long-range hydrodynamic interactions requires the solution of a many-body problem.

At distances large compared to the fibre diameter d, the velocity disturbance, u_α^f, created by fibre α can be expressed as a line distribution of forces, f_α, along the centre-line of the fibre

$$u_\alpha^f(x) = \int_{-L/2}^{L/2} J(x - x_\alpha - s p_\alpha) \cdot f_\alpha(s) \mathrm{d}s, \tag{2.6}$$

where $\boldsymbol{J}$ is the Oseen tensor

$$\boldsymbol{J}(\boldsymbol{y}) = \frac{1}{8\pi}\left(\frac{\boldsymbol{I}}{|\boldsymbol{y}|} + \frac{\boldsymbol{y}\boldsymbol{y}}{|\boldsymbol{y}|^3}\right).$$

The force distribution $\boldsymbol{f}_\alpha$ is found by imposing no slip at the surface of the fibre to an inner expansion for the fluid velocity, which is then matched to the outer solution given by (2.6) (Batchelor 1970). At leading order in $\log(2r)$, this matching leads to the following equation for $\boldsymbol{f}_\alpha$:

$$\dot{\boldsymbol{x}}_\alpha + s\boldsymbol{p}_\alpha - \boldsymbol{u} = \frac{\log(2r)}{4\pi}(\boldsymbol{I} + \boldsymbol{p}_\alpha\boldsymbol{p}_\alpha)\cdot\boldsymbol{f}_\alpha, \tag{2.7}$$

where $\boldsymbol{u}$ is the fluid velocity excluding the velocity disturbance caused by fibre α. We approximate $\boldsymbol{f}$ as a linear distribution,

$$\boldsymbol{f}_\alpha(s) = \frac{1}{L}\boldsymbol{F}_\alpha + \frac{12}{L^3}s(\boldsymbol{T}_\alpha \wedge \boldsymbol{p}_\alpha + S_\alpha\boldsymbol{p}_\alpha), \tag{2.8}$$

where

$$\boldsymbol{F}_\alpha = \int_{-L/2}^{L/2}\boldsymbol{f}_\alpha\mathrm{d}s, \quad \boldsymbol{T}_\alpha = \int_{-L/2}^{L/2}s\boldsymbol{p}_\alpha \wedge \boldsymbol{f}_\alpha\mathrm{d}s, \quad S_\alpha = \int_{-L/2}^{L/2}s\boldsymbol{p}_\alpha\cdot\boldsymbol{f}_\alpha\mathrm{d}s. \tag{2.9}$$

Because the inertia of the fibre is negligible, force and torque balances on the fibre require that the net hydrodynamic force $\boldsymbol{F}_\alpha$ and torque $\boldsymbol{T}_\alpha$ must be equal respectively to the net force and torque on the fibre due to contact forces. Thus we have

$$\boldsymbol{F}_\alpha = \sum N_k, \quad \boldsymbol{T}_\alpha = \boldsymbol{p}_\alpha \wedge \sum s_k N_k, \tag{2.10}$$

where N_k is the kth contact force and the sum is over all contacts on fibre α. The remaining term, S_α, represents the stresslet, caused by the resistance of the fibre to stretching. By forming the scalar product of equation (2.7) with $s\boldsymbol{p}_\alpha$ and integrating over the length of the fibre we obtain

$$S_\alpha = -\frac{2\pi}{\log(2r)}\int_{-L/2}^{L/2}\boldsymbol{u}\cdot\boldsymbol{p}_\alpha\mathrm{d}s. \tag{2.11}$$

This level of approximation is equivalent to the multi-particle interaction in the Stokesian dynamics simulations of Claeys & Brady. Their simulations were for finite-aspect-ratio spheroids and also included a two-body lubrication term, which we neglect on the grounds that lubrication forces are negligible for high-aspect-ratio particles, and the short-range interactions are controlled by mechanical contacts.

2.4. *Equations of motion for the system*

Combining equations (2.1)–(2.3) with equations (2.5)–(2.10), the velocity of the sphere and the translational and angular velocities of each fibre in the suspension can be written in terms of a weighted sum over the stresslets S_α on each fibre, the contact forces N_k and the sphere weight W,

$$\left.\begin{aligned}
\dot{\boldsymbol{x}}^{\mathrm{sph}} &= \frac{W}{3\pi\sigma} + \sum_k \boldsymbol{M}_{\mathrm{sph}}^k\cdot N_k + \sum_\beta \boldsymbol{P}_{\mathrm{sph}}^\beta S_\beta, \\
\dot{\boldsymbol{x}}_\alpha^{\mathrm{f}} &= \boldsymbol{K}_\alpha\cdot W + \sum_k \boldsymbol{M}_\alpha^k\cdot N_k + \sum_\beta \boldsymbol{P}_\alpha^\beta S_\beta, \\
\dot{\boldsymbol{p}}_\alpha^{\mathrm{f}} &= \boldsymbol{L}_\alpha\cdot W + \sum_k \boldsymbol{Q}_\alpha^k\cdot N_k + \sum_\beta \boldsymbol{R}_\alpha^\beta S_\beta.
\end{aligned}\right\} \tag{2.12}$$

The tensors $\boldsymbol{K}$ and $\boldsymbol{L}$ are found by integrating the velocity disturbance of the sphere (equation (2.5)) over the length of the fibres,

$$
\left.\begin{aligned}
\boldsymbol{K}_\alpha &= \frac{1}{L} \int_{-L/2}^{L/2} ds_\alpha \boldsymbol{H}(\boldsymbol{x}_\alpha + s_\alpha \boldsymbol{p}_\alpha - \boldsymbol{x}^{\mathrm{sph}}), \\
\boldsymbol{L}_\alpha &= \frac{12}{L^3}(\boldsymbol{I} - \boldsymbol{p}_\alpha \boldsymbol{p}_\alpha) \cdot \int_{-L/2}^{L/2} ds_\alpha s_\alpha \boldsymbol{H}(\boldsymbol{x}_\alpha + s_\alpha \boldsymbol{p}_\alpha - \boldsymbol{x}^{\mathrm{sph}}).
\end{aligned}\right\}
\tag{2.13}
$$

The mobility matrices $\boldsymbol{M}$ and $\boldsymbol{Q}$ include both the direct effect of the contact force on the two contacting particles, and its indirect effect on all the other particles due to the propagation of the disturbance through the fluid. To illustrate how these mobility functions are calculated, we consider a contact between fibres a and b, where the contact is at position $\boldsymbol{x}_a + \lambda_a^k \boldsymbol{p}_a = \boldsymbol{x}_b + \lambda_b^k \boldsymbol{p}_b$. The direct effect of this force on fibres a and b is given by equation (2.3), so that

$$
\left.\begin{aligned}
\boldsymbol{M}_a^k &= \frac{\log(2r)}{4\pi L}\boldsymbol{I}, \quad \boldsymbol{Q}_a^k = \frac{3\log(2r)}{\pi L^3}\lambda_a^k(\boldsymbol{I} - \boldsymbol{p}_a \boldsymbol{p}_a), \\
\boldsymbol{M}_b^k &= -\frac{\log(2r)}{4\pi L}\boldsymbol{I}, \quad \boldsymbol{Q}_a^k = -\frac{3\log(2r)}{\pi L^3}\lambda_b^k(\boldsymbol{I} - \boldsymbol{p}_b \boldsymbol{p}_b).
\end{aligned}\right\}
\tag{2.14}
$$

The indirect motion of the other fibres in the suspension is generated by the net force and torque on fibres a and b, and so from equations (2.6), (2.8), (2.10) we find that

$$
\begin{aligned}
\boldsymbol{M}_\alpha^k = \frac{1}{L^2} \int_{-L/2}^{L/2} ds_\alpha \Bigg\{ &\int_{-L/2}^{L/2} ds_a \left(1 + 12 s_a \lambda_a^k / L^2\right) \boldsymbol{J}(\boldsymbol{x}_\alpha + s_\alpha \boldsymbol{p}_\alpha - \boldsymbol{x}_a - s_a \boldsymbol{p}_a) \\
&- \int_{-L/2}^{L/2} ds_b \left(1 + 12 s_b \lambda_b^k / L^2\right) \boldsymbol{J}(\boldsymbol{x}_\alpha + s_\alpha \boldsymbol{p}_\alpha - \boldsymbol{x}_b - s_b \boldsymbol{p}_b)\Bigg\},
\end{aligned}
\tag{2.15a}
$$

$$
\begin{aligned}
\boldsymbol{Q}_\alpha^k = \frac{12}{L^4}(\boldsymbol{I} - \boldsymbol{p}_\alpha \boldsymbol{p}_\alpha) \cdot &\int_{-L/2}^{L/2} ds_\alpha s_\alpha \\
\times \Bigg\{ &\int_{-L/2}^{L/2} ds_a \left(1 + 12 s_a \lambda_a^k / L^2\right) \boldsymbol{J}(\boldsymbol{x}_\alpha + s_\alpha \boldsymbol{p}_\alpha - \boldsymbol{x}_a - s_a \boldsymbol{p}_a) \\
&- \int_{-L/2}^{L/2} ds_b \left(1 + 12 s_b \lambda_b^k / L^2\right) \boldsymbol{J}(\boldsymbol{x}_\alpha + s_\alpha \boldsymbol{p}_\alpha - \boldsymbol{x}_b - s_b \boldsymbol{p}_b)\Bigg\}.
\end{aligned}
\tag{2.15b}
$$

In each of these double integrals, the inner integrals over fibres a and b can be evaluated analytically (see Chwang & Wu 1975) leaving a single integral that must be performed numerically. This integral is evaluated using Simpson's rule with 6 intervals for fibres whose centres are more than one fibre length apart, and 10 intervals otherwise, giving a relative error of approximately 10^{-4}.

The contribution of this contact force to the velocity of the sphere may be calculated from the Faxén law (equation (2.1)), and is given by

$$
\begin{aligned}
\boldsymbol{M}_{\mathrm{sph}}^k = \frac{1}{L} \int_{-L/2}^{L/2} ds_a \left(1 + 12 s_a \lambda_a^k / L^2\right) \left(1 + \frac{\sigma^2}{24}\nabla_{\boldsymbol{x}^{\mathrm{sph}}}^2\right) \boldsymbol{J}(\boldsymbol{x}^{\mathrm{sph}} - \boldsymbol{x}_a - s_a \boldsymbol{p}_a) \\
-\frac{1}{L} \int_{-L/2}^{L/2} ds_b \left(1 + 12 s_b \lambda_b^k / L^2\right) \left(1 + \frac{\sigma^2}{24}\nabla_{\boldsymbol{x}^{\mathrm{sph}}}^2\right) \boldsymbol{J}(\boldsymbol{x}^{\mathrm{sph}} - \boldsymbol{x}_b - s_b \boldsymbol{p}_b).
\end{aligned}
\tag{2.16}
$$

In the case where the contact is between the sphere and a fibre, contributions

to $\boldsymbol{M}_\alpha^k$ and $\boldsymbol{Q}_\alpha^k$ from fibre a are replaced by the tensors $\boldsymbol{K}_\alpha$ and $\boldsymbol{L}_\alpha$ respectively and $\boldsymbol{M}_{sph}^k = \boldsymbol{I}/(3\pi\sigma)$.

The vectors $\boldsymbol{P}$ and $\boldsymbol{R}$ in equation (2.12) arise from the velocity disturbance created by the stresslet on fibre α, and are given by

$$\left.\begin{aligned} \boldsymbol{P}_\alpha^\beta &= \frac{12}{L^4} \int_{-L/2}^{L/2} \mathrm{d}s_\alpha \int_{-L/2}^{L/2} \mathrm{d}s_\beta s_\beta \boldsymbol{p}_\beta \cdot \boldsymbol{J}(\boldsymbol{x}_\alpha + s_\alpha \boldsymbol{p}_\alpha - \boldsymbol{x}_\beta - s_\beta \boldsymbol{p}_\beta) \\ \boldsymbol{R}_\alpha^\beta &= \frac{144}{L^6}(\boldsymbol{I} - \boldsymbol{p}_\alpha \boldsymbol{p}_\alpha) \cdot \int_{-L/2}^{L/2} \mathrm{d}s_\alpha s_\alpha \int_{-L/2}^{L/2} \mathrm{d}s_\beta s_\beta \boldsymbol{J}(\boldsymbol{x}_\alpha + s_\alpha \boldsymbol{p}_\alpha - \boldsymbol{x}_\beta - s_\beta \boldsymbol{p}_\beta) \cdot \boldsymbol{p}_\beta \end{aligned}\right\} \quad (2.17)$$

As before, the inner integral over fibre β may be evaluated analytically while the outer integral is computed numerically.

Finally, the vector $\boldsymbol{P}_{sph}^\beta$ is formed by applying Faxén's law (equation (2.1)) to the velocity disturbance created by the stresslet on fibre β, so that

$$\boldsymbol{P}_{sph}^\beta = \frac{12}{L^3} \int_{-L/2}^{L/2} \mathrm{d}s_\beta s_\beta \left(1 + \frac{\sigma^2}{24}\nabla_{\boldsymbol{x}^{sph}}^2\right) \boldsymbol{p}_\beta \cdot \boldsymbol{J}(\boldsymbol{x}^{sph} - \boldsymbol{x}_\beta - s_\beta \boldsymbol{p}_\beta). \quad (2.18)$$

This integral was calculated numerically using the method described above.

By substituting the expressions for $\dot{\boldsymbol{x}}$ and $\dot{\boldsymbol{p}}$ into equation (2.4) we obtain an equation involving the contact forces and stresslets, for each contact. Equation (2.11) provides an equation for the stresslet on each fibre. Thus we obtain a full system of linear equations for the magnitude of the contact forces N_k and the stresslets S, which are then solved using Crout elimination.

As noted above an additional constraint on the system is that all the contact forces must be positive. Therefore, if any of the forces N_k is found to be negative, the corresponding contact must be removed and the solution is recalculated.

Once the forces and stresslets have been calculated, the velocities and angular velocities of all the particles can be found from equation (2.12). The configuration of the system is then stepped forward in time until the next contact is made or broken (or to a maximum timestep of $3\pi\sigma L/40|\boldsymbol{W}|$ if there is no change in contacts within this timestep).

The main computational cost in these simulations is in constructing and solving the system of linear equations for the contact forces and stresslets. The computational time required for each timestep increases as the cube of the number of fibres, and the time between collisions decreases as the concentration increases. Consequently we are unable to simulate concentrations above nL^3 of 12, as these required 36 hours of CPU time on one node of the SP-2 supercomputer for each realization.

2.5. *Simulations without hydrodynamic interactions*

In order to investigate higher fibre number densities than are possible with hydrodynamic interactions, we performed some simulations with just contact forces. In these simulations the fibres do not move until they are struck by the sphere or by another fibre. Thus at any one time, only the cluster of fibres around the sphere that are connected through contacting fibres are moving. This greatly reduces the effort of searching for contacts, since at least one member of the fibre pair must be moving. Furthermore, only the contact forces N_k between fibres in the cluster need be computed. This greatly reduces the computational cost enabling simulations of suspensions with nL^3 in excess of 100 to be performed on a workstation.
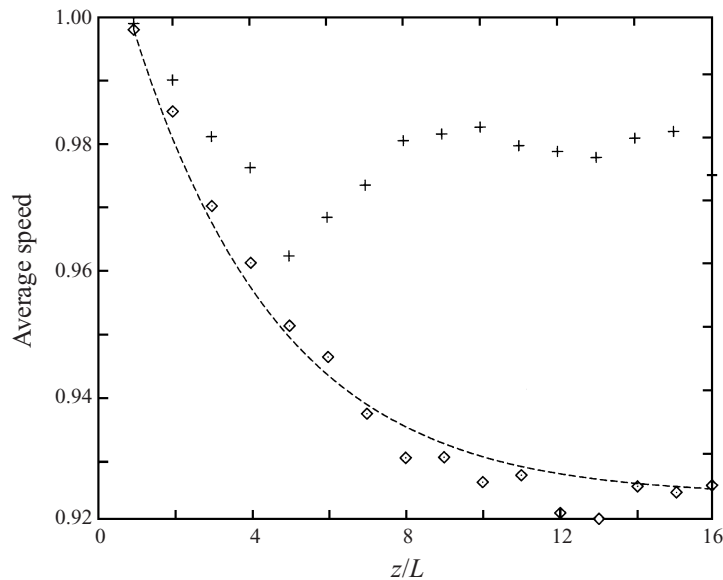
FIGURE 3. Plot of the average speed (from 25 realizations) of the sphere during the first 16 fibre lengths of its descent for $nL^3 = 1.2$; $\diamond$, excluding long-range hydrodynamic interactions; $+$, including long-range hydrodynamic interactions. The dashed curve indicates an exponential decay with an e-folding distance of $3.8L$.

3. Drag coefficient on a sphere of diameter $0.5L$

In this section and the next we discuss the results for the mean drag coefficient on the sphere. Throughout this section the sphere diameter, σ, and the fibre aspect ratio will be fixed at $0.5L$ and 20 respectively. These particular parameter values were chosen in order to provide a direct comparison with Milliken *et al.*'s experiments. The effects of varying the sphere size and fibre aspect ratio are discussed in the next section, where we present an asymptotic theory for spheres whose diameter is small compared to the fibre length.

The simulations were started with the sphere above a column of suspended fibres. For the smaller concentrations of fibres, $nL^3 \leqslant 1$, the column was 64 fibre lengths high with a square cross-section of 6×6 fibre lengths. For the higher concentrations the height of the column was reduced to 32 fibre lengths. For the simulations with random initial alignment, the fibres were positioned randomly with random orientations within the column. In the simulations with initially aligned suspensions, only the positions of the fibres were assigned at random. The simulations of suspensions without hydrodynamic interactions used columns that were 8×8 fibre lengths, in order to capture the full horizontal extent of the cluster of fibres around the sphere formed at higher fibre concentrations.

3.1. Initial motion

Although the fibres are initially randomly oriented and distributed throughout the column, as the sphere falls it produces local inhomogeneities in the orientational and spatial distribution of fibres near the sphere. These structures do not develop fully until the sphere has fallen some distance, and so the first few diameters of the sphere's descent are not typical of the remainder of its descent through the column. The speed of the sphere during the first 16 fibre lengths of its descent
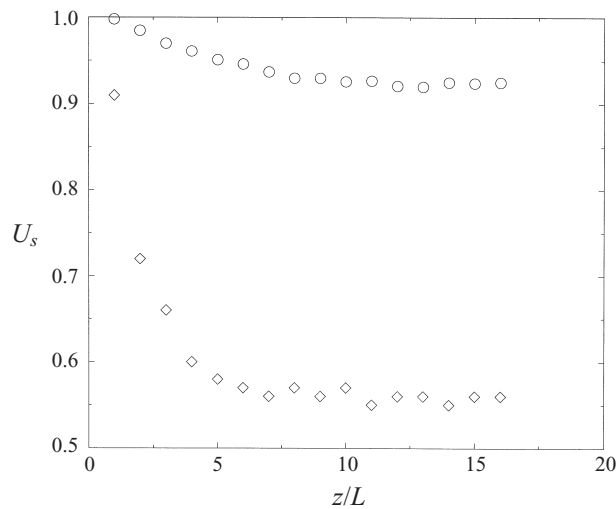
FIGURE 4. Plot of the average speed (from 25 realizations) of the sphere during the first 16 fibre lengths of its descent for different fibre concentrations: ○, $nL^3 = 1.14$; ◇, $nL^3 = 11.4$. Both simulations exclude long-range hydrodynamic interactions.

(averaged over 25 realizations and scaled with the sedimentation speed of an isolated sphere) is shown in figure 3 for nL^3 of 1.2 for simulations both with and without hydrodynamic interactions. In simulations without hydrodynamic interactions the average speed of the sphere decreases from unity to the equilibrium fall speed via an approximately exponential decay, with an e-folding distance of $3.8L$. We call this e-folding distance the 'entrance length'. This decrease in sedimentation speed with height is due to the compression of the fibres below the sphere as it falls through the suspension, enhancing the concentration of fibres in the region just below the sphere. Figure 4 shows that this entrance length varies with fibre concentrations. As the fibre concentration increases there is a very slight decrease in the entrance length, from an e-folding distance of approximately $4L$ to $3L$ as nL^3 increases from 1.14 to 11.4. This is because, as the concentration decreases, the frequency of collisions decreases, thus making the entrance length grow with decreasing concentration.

When long-range hydrodynamic interactions are included, as in the case of the data denoted by + symbols in figure 3, the speed of the sphere first decreases with distance but then increases again. This subsequent increase is due to the velocity disturbance from the sphere, which tends to displace fibres from the region below the sphere, and so reduce the frequency of collisions.

3.2. *Variation in mean drag coefficient with fibre concentration*

From figure 3 it can be seen that the sedimentation velocity reaches its equilibrium value after approximately 10 fibre lengths, and so in calculating the average sedimentation velocity of the sphere we neglect the first 10 fibre lengths of its fall. We also neglect the last 5 fibre lengths due to similar end effects at the bottom of the column. The effective drag coefficient, C_d, is defined as the ratio of the Stokes sedimentation speed to the average settling speed of the sphere U_{ave} through the remaining section of the column

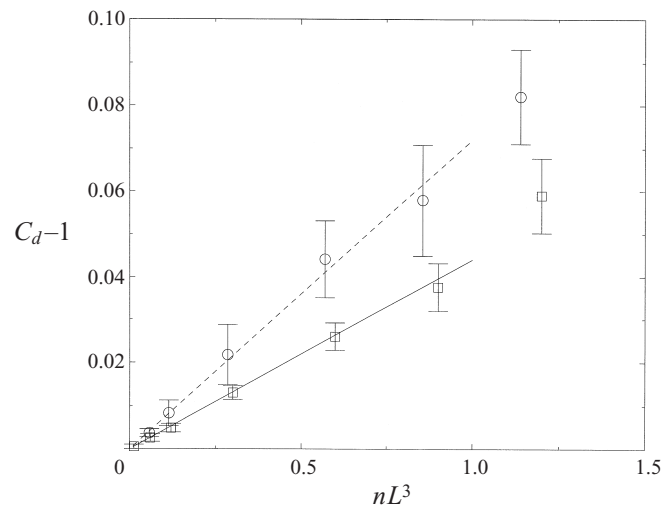$$C_d = \frac{|\boldsymbol{W}|}{3\pi\sigma U_{\text{ave}}}$$

FIGURE 5. Plot of $C_d - 1$ as function of nL^3 up to nL^3 of unity for a sphere of diameter $0.5L$ and a fibre aspect ratio of 20. The square symbols are simulations with hydrodynamic interactions and the solid line indicates $0.044nL^3$, the asymptote for small nL^3. The circles are simulations without hydrodynamics interactions and the dotted line is the corresponding small nL^3 asymptote of $0.072nL^3$. The error bars indicate 90% confidence intervals.

The results from the 25 different realizations (10 for nL^3 greater than unity) were combined for each combination of sphere diameter and fibre concentration to provide a mean value for the drag coefficient together with an error estimate (calculated as the 90% confidence interval). Fewer initial conditions are required at higher concentrations due to the increased number of fibre–sphere interactions within each realization.

Figure 5 shows the drag coefficient obtained from the simulations with and without hydrodynamic interactions for initially random suspensions up to nL^3 of unity. At these dilute concentrations the drag coefficient increases linearly with nL^3 as $1 + 0.044nL^3$ in the simulations that include hydrodynamic interactions. At low concentrations the sphere interacts with one fibre at a time, so that the extra hindrance caused by short-range interactions is proportional to the number of fibres encountered by the sphere, and therefore increases linearly with n. At these concentrations the effect of the long-range interactions is also linear in nL^3 as multifibre hydrodynamic interactions become important only for $nL^3 > 32$ (Mackaplow & Shaqfeh 1996).

The drag coefficients in the simulations without hydrodynamic interactions are also linear in nL^3 (with $C_d - 1 \simeq 0.072nL^3$), but are about 60% higher than found when hydrodynamic interactions are included. As noted above, the velocity disturbance caused by the sphere tends to push fibres away from the sphere, so that it clears a path for itself. Without hydrodynamic interactions, the only way the sphere can remove fibres from its path is to push them aside via direct mechanical contact, leading to an increase in the number and severity of collisions.

Above nL^3 of unity the drag coefficient rises more rapidly than the dilute asymptote, (see figure 6). This nonlinear increase in drag is mirrored by a corresponding increase in the average number of fibres contacting the sphere, either directly, or as part of a cluster in contact with the sphere, which is shown in figure 7. At small concentrations the sphere collides with individual fibres one at a time, and consequently the collision frequency and hence the average number of fibre contacts grows linearly with nL^3.
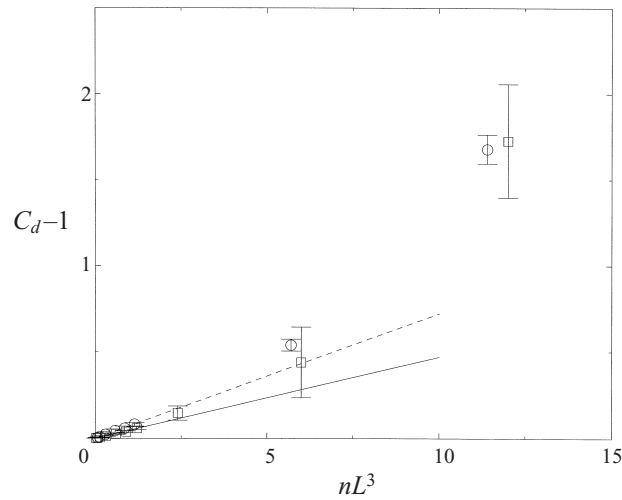
FIGURE 6. Plot of $C_d - 1$ as function of nL^3 up to nL^3 of 12 showing the departure from linear behaviour at around nL^3 of 2. The key is the same as in figure 5.
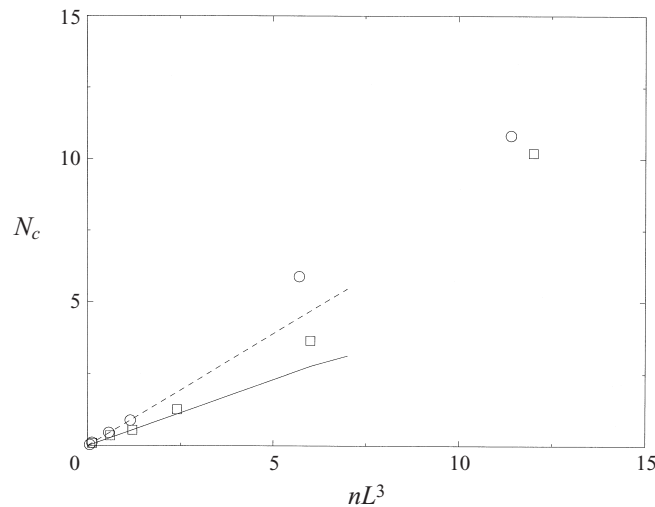

FIGURE 7. Plot showing the average number of fibres in contact with the sphere – either directly or as a part of cluster in contact with the sphere – as function of nL^3. The square symbols are simulations with hydrodynamic interactions and the solid line indicates $0.5nL^3$, the asymptote for small nL^3. The circles are for simulations without hydrodynamics interactions and the dotted line is the corresponding small nL^3 asymptote of $0.9nL^3$.

At a concentration around nL^3 of 2, the average number of contacting fibres reaches unity, indicating that at times more than one fibre is in contact with the sphere. Further increases in nL^3 produce a more rapid increase in the number of contacts. The nonlinear increase in drag also occurs around $nL^3 = 2$, indicating that this increase is due to multifibre contacts.

There are two separate effects that contribute to the nonlinear increase in the number of collisions. First, the growing cluster of fibres around the sphere increases its effective size as it falls through the suspension. Second, the high concentration of fibres impedes the ability of the sphere's velocity disturbance to remove fibres
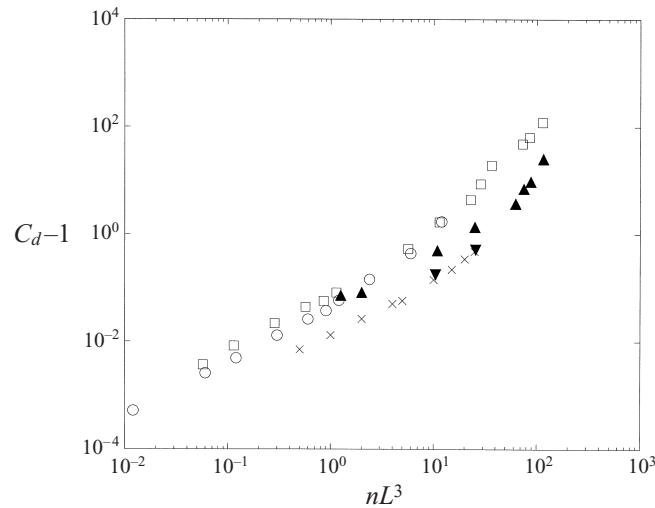
FIGURE 8. Comparison of drag coefficients between experiments and simulations for initially random and initially aligned suspensions. For initially random suspensions: ∘, simulations including hydrodynamic interactions; □, simulations without hydrodynamic interaction; ▲, experimental measurements of Milliken *et al*. For suspensions in which the fibres are initially all aligned vertically: (×), simulations including hydrodynamic interactions; ▼, experimental measurements by Mondy *et al*.

from its path. This latter effect can be seen by comparing the average number of contacts in simulations with and without hydrodynamic interactions in figure 7. At low concentrations there are almost twice as many contacts in the simulations without hydrodynamic interactions compared to simulations where these interactions are included, whereas at $nL^3 = 12$ the number of contacts is almost the same.

For this reason, the discrepancy between the simulations with and without hydrodynamic interactions reduces as we enter the semi-dilute regime, with no significant difference between the results at $nL^3 = 12$. This suggest that long-range hydrodynamic forces are progressively less important in governing the dynamics of the system as the fibre concentration increases, and that for fibre concentrations above nL^3 of 10 the dynamics are almost entirely controlled by short-range forces.

Figure 8 shows a comparison between the drag coefficients obtained from simulations with (∘) and without hydrodynamic interactions (□)and those measured in the experiments of Milliken *et al*. (▲). For $nL^3 < 10$ the results are in reasonably good agreement. However, in the simulations, the transition to nonlinear behaviour occurs around $nL^3 = 2$, while in the experiments this transition does not occur until nL^3 of around 50.

Also shown on this graph are the results (×) from simulations with initially vertically aligned suspensions. All these simulations include hydrodynamic interactions. The additional drag coefficient is found to increase as $0.013nL^3$, a factor of 3.3 lower than for a randomly oriented suspension and equal to the value found by Rosenberg *et al*. for a dilute suspension. This is not unexpected, as the sphere has fewer mechanical contacts so that its motion is not significantly hindered by collisions with fibres. The agreement with Rosenberg's results suggests that non-local hydrodynamic effects are small. Non-local effects are absent in Rosenberg's model, but are included in our simulations through the integral of the velocity over the fibre length.

In addition, unlike the randomly oriented suspension there is no transition to nonlinear behaviour once nL^3 exceeds 2. The dilute asymptote remains within the error bounds of the drag coefficient for nL^3 up to 20. The linearity of the drag with fibre concentration is consistent with purely hydrodynamic interactions. Hydrodynamic interactions alone only produce a weak logarithmic nonlinearity in viscosity for $nL^3 > 32$ (Mackaplow & Shaqfeh 1996). Consequently the nonlinear behaviour seen in the initially randomly aligned suspensions is due to collisions. The two data points from experimental measurements on an initially aligned suspension by Mondy *et al.* (▼) are slightly higher than the values found in the simulations, but follow the same trend.

There are a number possible explanations for the discrepancy between our simulations and the experimental measurements. The calculations use slender-body theory and a far-field approximation to the hydrodynamic interactions. Although the results of Mackaplow & Shaqfeh suggest that this should be an adequate representation for these values of nL^3, there may be important errors in hydrodynamic interactions at distances of less than one fibre length. As well as these approximations in the theory, the experiments may also not be ideal. It can be seen from figure 8 that the experimental measurements for both random and initially aligned suspensions lie between the results from simulations on initially aligned suspensions and those on initially randomly oriented suspensions. This suggests that one explanation for the discrepancy between the experiments and simulations is that it is not possible to produce perfect initial orientation distributions in experiment. In Mondy's experiments the fibres were aligned by moving a porous mesh up and down through the suspension, so that the alignment is induced hydrodynamically. If this alignment is not perfect, the sphere has a chance to collide with more fibres on average, thereby experiencing a higher drag. Similarly the initial orientation distribution in Milliken *et al.*'s experiments was produced by stirring the suspension, and particularly at higher concentrations this may not produce a truly random orientation distribution. Either preferred fibre alignment parallel to the direction of gravity or correlation in the local alignment of fibres would decrease the drag, and delay the transition to nonlinear behaviour.

At higher fibre concentrations there is also the possibility that fibres in the experiments will bend under the high stresses generated by the sphere. Although Milliken *et al.* concluded that fibre bending was negligible, their estimate was based on the magnitude of the hydrodynamic force created by the falling sphere. However, in a suspension where multi-fibre contacts are prevalent, substantially larger torques may be generated. As a worst case scenario, we consider a horizontal fibre, with one end trapped by surrounding fibres, and the net weight of the sphere $W = \pi\sigma^3 g(\rho_b - \rho_{fl})/6$ acting on the other end (where ρ_b and ρ_{fl} are respectively the density of the sphere ($8.7 \times 10^3\,\text{kg}\,\text{m}^{-3}$) and the fluid ($1.18 \times 10^3\,\text{kg}\,\text{m}^{-3}$). The bending of this fibre can be estimated from beam theory (Shames 1979) in terms of the radius of curvature, R, of the deformed fibre. For small deformations, R is given by

$$\frac{E\pi d^4}{64R} = WL,$$

where E is the Young's modulus of the fibre (equal to $3 \times 10^9\,\text{N}\,\text{m}^{-2}$ for the PMMA fibres used in the experiment), d is the diameter of the fibres (1.6 mm). For $0.3 < \sigma/L < 0.5$, we find that $12 > R/L > 4$, indicating that the torques generated in a contacting suspension are large enough to produce significant bending of the fibres. Fibre bending may be an important mechanism for releasing a sphere that is blocked by a cage of contacting fibres, thereby reducing the effective viscosity.
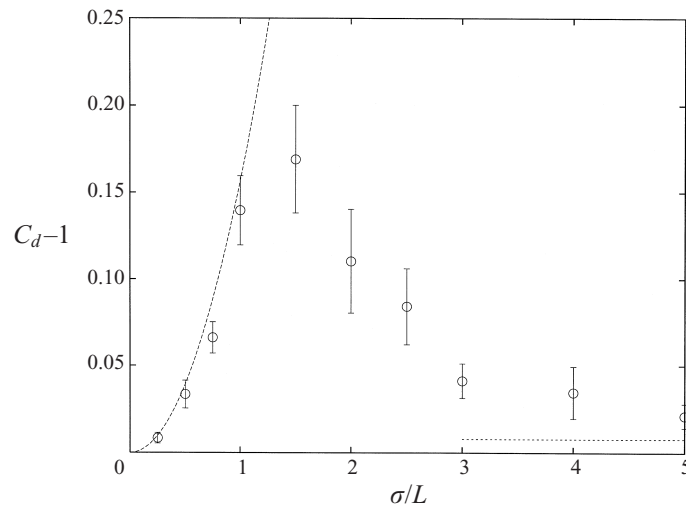
FIGURE 9. Plot of the variation in the additional drag coefficient with sphere diameter for $nL^3 = 0.6$ for simulations without hydrodynamic interactions. The dashed curve denotes the asymptotic behaviour for $\sigma/L \ll 1$, given by equation (4.6), while the dotted line represents $C_d - 1 = 0.013nL^3$ the result found by Rosenberg *et al.* that corresponds to the limit $\sigma/L \to \infty$.

4. Dependence on sphere diameter

We now consider the effect of varying the sphere diameter to fibre length ratio, σ/L. The variation of the drag coefficient with sphere diameter is shown in figure 9 for a fibre concentration of $nL^3 = 0.6$ for simulations without hydrodynamic interactions. This shows that the drag coefficient increases with sphere diameter up to a maximum drag for spheres between 1 and 2 fibre lengths in diameter, followed by a decrease towards an asymptote for large spheres.

A sphere whose radius is small compared with the fibres can move more easily through the suspension without colliding with many fibres. For small σ/L the frequency of collisions with fibres will be proportional to $nL\sigma U_s$, while the distance the sphere has to move horizontally to get around the fibre is proportional to σ; consequently the drag coefficient should increase with the square of the sphere diameter. This limit of small sphere diameter to fibre length is considered in more detail in §4.2.

In the opposite limit where the sphere diameter is large compared to the fibre length the dynamics are dominated by the long-range hydrodynamic disturbance of the sphere. This disturbance will be linear on the lengthscale of the fibres, and so collisions between fibres will be rare in a semi-dilute suspension. On the length scale of the sphere the suspension may be treated as a continuum, and this is the limit in which Rosenberg's calculations apply. As the sphere decreases in size relative to the fibres, the flow becomes more nonlinear and collisions become more frequent. This causes the drag coefficient to increase. The largest values of the drag coefficient occur for sphere sizes intermediate between these two extremes, when the sphere diameter is comparable to the length of the fibres.

At higher concentrations, such as $nL^3 = 11.4$ shown in figure 10, the variation in drag coefficient follows the same pattern as at lower concentrations, but the peak in the drag coefficient at intermediate concentrations is broader. The increased density of fibres makes it more difficult for a small sphere to fall through the gaps between the
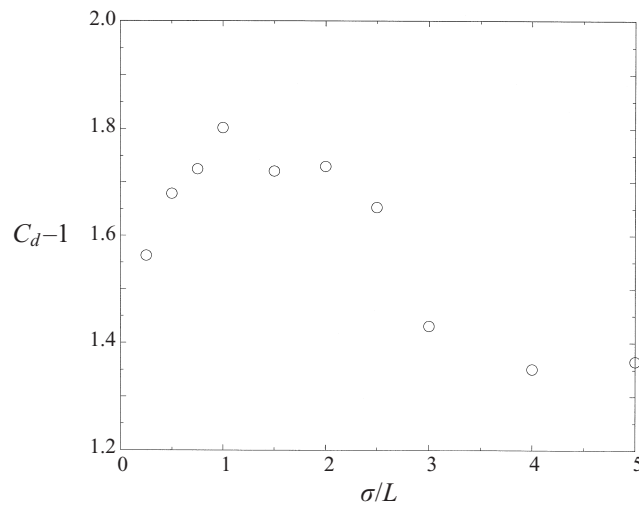
FIGURE 10. Plot of the variation in the additional drag coefficient with sphere diameter for $nL^3 = 11.4$ for simulations without hydrodynamic interactions.

fibres so that the small σ/L limit only applies for very small spheres, $\sigma/L \ll (nL^3)^{-1/2}$, since the typical spacing between fibres in the suspension is $(nL)^{-1/2}$.

In their experiments, Milliken *et al.* used a limited range of sphere sizes with diameters in the range 0.3–0.7L and found no detectable change in drag coefficient with σ/L. In figure 10 it can be seen that there is only about a 10% variation in drag over this range of sphere sizes. In later experiments Powell *et al.* considered a larger range of sphere sizes and observed a decrease in drag coefficient with sphere diameter for σ less than 0.3L. From their results, Powell *et al.* concluded that spheres with diameters of around 0.5L are large enough to obtain the asymptotic result for large spheres. In contrast our results indicate that this limit is not reached until the sphere diameter is at least 5 times the fibre length.

For spheres of diameter 5 and 10 fibre lengths, Ralambotiana *et al.* (1997) find much smaller increases in the drag coefficient with fibre concentration than reported by Milliken *et al.* and Powell *et al.* For fibre concentrations below nL^3 of 20, the drag coefficient in Ralambotiana *et al.*'s experiments increases linearly with nL^3 in the range $0.008nL^3$ to $0.025nL^3$, depending upon the fibre aspect ratio. Furthermore the results for different fibre aspect ratio superimpose when plotted against nL^2d rather than nL^3. This apparent discrepancy between these two sets of experiments suggests that the drag coefficient on a sphere of the order of a fibre length in diameter is much larger than on a sphere whose diameter is large compared to the length of the fibres.

4.1. *Effect of varying fibre aspect ratio*

In their experiments Powell *et al.* (see figure 1) find no significant difference between fibres of different aspect ratios for a limited range of aspect ratios of 20 to 50. For high-aspect-ratio particles the collision cross-section of a fibre is determined at leading order by its length, so that the aspect ratio does not directly affect the frequency of collisions. However, the aspect ratio does affect the dynamics of the suspension because the mobility of a fibre is proportional to $1/\log(2r)$.

In the limit of small spheres, $\sigma \ll L$, the mobility of the sphere is large compared to that of the fibres, so that the fibres remain fixed while the sphere migrates through the gaps in between the fibres. Thus in this limit we would expect the drag to be
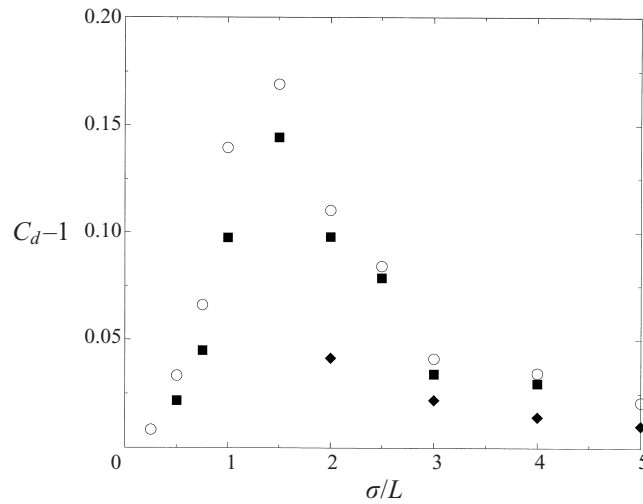
FIGURE 11. Plot of the variation in the additional drag coefficient with sphere diameter and fibre aspect ratio for simulations without hydrodynamic interactions at $nL^3 = 0.6$: ∘, $r = 20$; ■, $r = 50$; ◆, $r = 50$.

independent of the fibre aspect ratio. In the opposite limit, where the sphere diameter is large compared to the fibre length, the mobility of the fibres is large compared to that of the sphere, so that the increase in drag coefficient would be expected to be proportional to $1/\log(2r)$. This suggests that at intermediate values of σ/L the dependence on aspect ratio is weaker than $1/\log(2r)$, with the largest differences occurring for $\sigma \gg L$.

Results for the drag coefficient for fibre aspect ratios ranging from $r = 20$ to 500 are shown in figure 11. Simulations for the highest aspect ratio, $r = 500$, were only performed for $\sigma/L \geqslant 2$. It can be seen that the drag coefficient decreases with aspect ratio. Furthermore, the ratio of the drag coefficient corresponding to $L/d = 500$ to that for $L/d = 20$ ranges from 0.37 to 0.48, which is comparable to and slightly smaller than, $\log(2 \times 20)/\log(2 \times 100) = 0.53$.

4.2. *Asymptotic theory for small spheres*

We now consider in greater detail the limit where the ball diameter is small compared to the fibre length, L (but still large compared to the fibre diameter). In this limit the resistivity of the fibres will be large compared to that of the sphere and so the sphere will not displace the fibres. Instead, the sphere will move around the fibre until it can continue its vertical descent.

We consider the motion of a sphere of radius a ($= \sigma/2$) in collision with a fibre of length L and diameter d, such that $d \ll a \ll L$. We define θ to be the angle between the fibre axis and the vertical, and choose Cartesian coordinates (x, y, z) with the z-axis parallel to the fibre and the x-axis as the horizontal axis in the plane perpendicular to the fibre (see figure 12). In this coordinate system the gravitational force on the sphere is

$$\boldsymbol{W} = (0, -W \sin \theta, W \cos \theta).$$

The reaction force, $\boldsymbol{N}$, acts along the line in the (x, y)-plane through the fibre and the centre of the sphere, and so has components

$$\boldsymbol{N} = N(\cos \phi, \sin \phi, 0) \quad \text{where } \phi = \cos^{-1}(X/a),$$
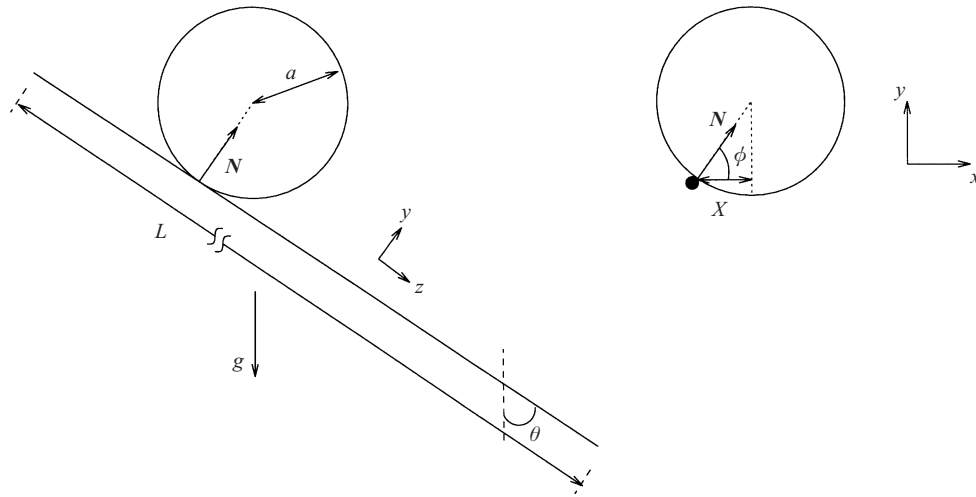
FIGURE 12. Sketch showing the coordinate system, (x, y, z), used to calculate the motion of the sphere in the limit where the sphere diameter is small compared to the fibre length.

and X is the (minimum) horizontal distance between the sphere centre and the fibre axis.

Since the fibre remains fixed, the sphere can have no motion in the direction normal to the fibre, so that $N = W \sin\theta \sin\phi$. Hence the velocity of the sphere is given by

$$U_0 \left[(X/a)(1 - (X/a)^2)^{1/2} \sin\theta, \; -(X/a)^2 \sin\theta, \cos\theta \right], \quad (4.1)$$

where U_0 is the unhindered sedimentation speed of the sphere. The downward vertical component of the sphere's velocity is now

$$U_0(\cos^2\theta + (X/a)^2 \sin^2\theta),$$

so that, compared to an unhindered sphere falling at U_0, an additional time of

$$\Delta T = \int (1 - (X/a)^2) \sin^2\theta \, \mathrm{d}t$$

is required to by-pass this fibre. From equation (4.1), we observe that

$$\frac{\mathrm{d}X}{\mathrm{d}t} = U_0(X/a)(1 - (X/a)^2)^{1/2} \sin\theta$$

and so the additional time is given by

$$\Delta T(X_0, \theta) = \frac{a}{U_0} \sin\theta \, K(X_0/a), \quad (4.2)$$

where X_0 is the value of X when the sphere first hits the fibre and

$$K(x) = \int_x^1 \frac{(1 - x^2)^{1/2}}{x} \mathrm{d}x$$

$$= (1 - x^2)^{1/2} + \log x - \log\left(1 - (1 - x^2)^{1/2}\right). \quad (4.3)$$

Under the assumption that the sphere only interacts with one fibre at a time, the average speed of descent of the sphere through a depth, H, of the suspension will be

$$U_s = \frac{U_0}{1 + (U_0/H)\sum_i \Delta T_i},$$

where the index i represents the individual collisions. The collision cross-section of a fibre at angle θ is equal to $2La\sin\theta$, so that for $H \gg 1/nLa$

$$\frac{U_0}{H}\sum_i \Delta T_i \sim 2nLU_0 \int_\Omega \mathrm{d}\Omega P(\Omega) \int_0^a \mathrm{d}X \Delta T(X_0, \theta), \qquad (4.4)$$

where the integral over Ω denotes integration over the surface of the unit sphere and $P(\Omega)$ is the fibre orientation distribution. For an isotropic orientation distribution, $P = 1/4\pi$, and equation (4.4) can be evaluated by integration by parts to give

$$\frac{U_0}{H}\sum_i \Delta T_i \sim 2nLa \int_0^{\pi/2} \sin^3\theta\,\mathrm{d}\theta \int_0^a \mathrm{d}X \int_X^a \mathrm{d}X' \frac{(1 - (X'/a)^2)^{1/2}}{X'} = \frac{nLa^2\pi}{3}. \qquad (4.5)$$

Thus, in the limit $1/r \ll \sigma/L \ll 1$, the drag coefficient on the sphere is given by

$$C_d \sim 1 + \frac{nL\sigma^2\pi}{12}. \qquad (4.6)$$

The assumption that the sphere only interacts with one fibre at a time further restricts this result to $1/r \ll \sigma/L \ll (nL^3)^{-1/2}$, so that this regime only exists for small volume fraction. The curve given by equation (4.6) is shown on figure 9 and is within the error bars for σ/L up to 0.5. Equation (4.6) over-predicts the drag as σ/L increases, because of the assumption that the fibres do not move during the collision. At finite σ/L the force of the sphere on the fibre will tend to move the fibre out of the way, thereby reducing ΔT.

5. Effective diffusivity of the sphere

In addition to the effect on the mean sedimentation speed of the sphere, the random nature of the interactions with the fibres will give rise to an effective diffusion of the sphere about this mean vertical sedimentation. This diffusion can by represented via an effective diffusivity tensor $\boldsymbol{D}$ defined as

$$\boldsymbol{D} = \frac{1}{2}\frac{\mathrm{d}}{\mathrm{d}t}\langle(\boldsymbol{x}_\mathrm{s} - \langle\boldsymbol{U}_\mathrm{s}\rangle t)(\boldsymbol{x}_\mathrm{s} - \langle\boldsymbol{U}_\mathrm{s}\rangle t), \qquad (5.1)$$

where $\boldsymbol{x}_\mathrm{s}$ is the displacement of the sphere from its original starting position. From the symmetry of the flow this tensor must be axisymmetric about the vertical direction and so we need only determine the components of $\boldsymbol{D}$ that correspond to diffusion in the vertical and horizontal directions, D_v and D_h respectively, where

$$\boldsymbol{D} = D_\mathrm{v}\boldsymbol{KK} + D_\mathrm{h}(\boldsymbol{I} - \boldsymbol{KK})$$

and $\boldsymbol{K}$ is the unit vector in the vertical direction.

From equation (5.1), the horizontal distance, r, of the sphere from its starting position grows as

$$\langle r^2 \rangle = 4D_\mathrm{h}t \qquad (5.2)$$

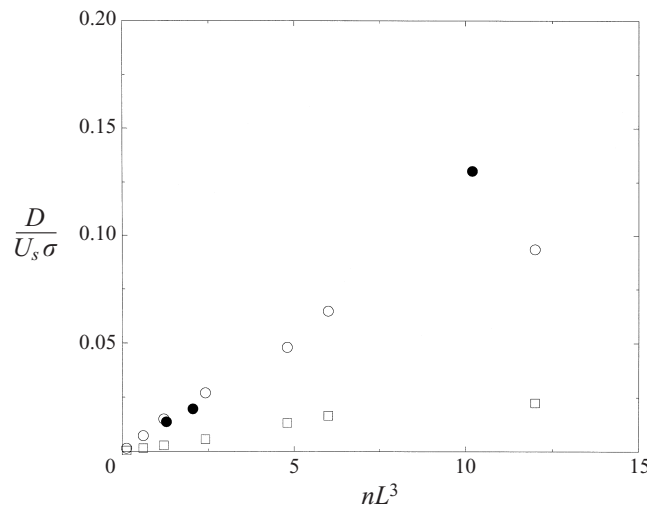and so by measuring the horizontal distance moved by the sphere during its descent

FIGURE 13. Plot of the vertical and horizontal diffusivity of the sphere scaled by its sedimentation speed and diameter, as a function of nL^3: ○, vertical diffusivity for $\sigma = 0.2L$; □, horizontal diffusivity for $\sigma = 0.2L$. The filled circles show experimental values of vertical diffusivity determined by Abbott *et al.* from the data of Milliken *et al.*

and averaging over the different realizations we can calculate D_h from the simulations. Similarly, the vertical diffusivity can be calculated from the variance of the vertical distance fallen as

$$\langle (z - U_s t)^2 \rangle = 2 D_v t. \tag{5.3}$$

The values of D_h and D_v for simulations including hydrodynamic interactions for $\sigma = 0.2L$ are plotted in figure 13. Since diffusivity has units of velocity multiplied by length, we have chosen to use dimensions of $U_s \sigma$. The vertical diffusivity is found to be approximately 5 times the diffusivity in the horizontal direction, and both components vary linearly with nL^3, as $0.01nL^3 U_s \sigma$ and $0.002nL^3 U_s \sigma$ respectively, at least for values of nL^3 up to 5. The slower than linear growth of $\boldsymbol{D}$ with nL^3 at higher concentrations ($nL^3 > 10$) probably results from hindering of the displacement of the ball caused by one fibre due to concurrent contacts between the ball and other fibres.

Experimental measurements of the vertical diffusivity have been obtained by Abbott *et al.* (1998) from the variance in the settling times recorded by Milliken *et al.* These values are plotted as filled circles in figure 13. The standard deviation in the experimental measurements is between one half and one third of the mean value. For the two lowest concentrations the agreement between the experimental values and our calculations is better than should be expected given the uncertainty in the experimental values. The value at $nL^3 = 10$ is about 50% higher than our calculations, and does not show the deviation from linear growth seen in the calculations.

As with the drag coefficient in the previous section we can calculate the components of the diffusivity in the limit $\sigma/L \ll 1$ using the asymptotic theory developed in §4.2. Each collision with a fibre produces a horizontal displacement δ_h and a vertical displacement δ_v to the path of the sphere.

The horizontal displacement during each collision may be resolved into components parallel and perpendicular to the fibre axis. The component of the sphere's velocity parallel to the horizontal projection of the fibre axis is

$$U_0 \sin \theta \cos \theta (1 - (X/a)^2),$$

so that the displacement in this direction is

$$\delta_1 = \int_{X_0}^{a} U_0 \cos\theta \sin\theta \, (1 - (X/a)^2) \mathrm{d}t = a\cos\theta\, K(X_0/a).$$

The displacement perpendicular to the fibre, δ_2, is simply $a - X_0$, so that a collision with a fibre at angle θ and offset X_0 produces a squared horizontal displacement of

$$\delta_h^2 = (a - X_0)^2 + a^2 \cos^2\theta \left[K(X_0/a)\right]^2.$$

Since each collision is uncorrelated with the others, the mean-square horizontal displacement of the fibre in falling through a height H is given by

$$\langle r^2 \rangle = 2nHLa \int_0^{\pi/2} \mathrm{d}\theta \sin^2\theta \int_0^a \mathrm{d}X_0 \delta_h^2.$$

The sphere takes a time H/U_s to fall this distance and so

$$\begin{aligned} D_h &= \frac{nU_sLa}{2} \int_0^{\pi/2} \mathrm{d}\theta \sin^2\theta \int_0^a \mathrm{d}X_0 \delta_h^2 \\ &= \frac{nU_sLa\pi}{32} \int_0^a \mathrm{d}X_0 4(a - X_0)^2 + \left[K(X_0/a)\right]^2 \\ &= 0.03475 nLU_s\sigma^3 \end{aligned} \tag{5.4}$$

The vertical displacement δ_v may be calculated directly from ΔT, the extra time required to by-pass the fibre, as $\delta_v = U_0 \Delta T$, so that from equation (4.2)

$$\delta_v(X_0, \theta) = a\sin\theta\, K(X_0/a).$$

The vertical diffusivity is therefore given by

$$\begin{aligned} D_v &= nLa^3 U_s \int_0^{\pi/2} \mathrm{d}\theta \sin^4\theta \int_0^1 \mathrm{d}z K(z)^2, \\ &= 0.1103 U_s nL\sigma^3. \end{aligned} \tag{5.5}$$

For $\sigma/L = 0.2$, the small-ball theory, which neglects hydrodynamic interactions, yields horizontal and vertical diffusivities of $0.0014 nL^3 U_s\sigma$ and $0.0044 nL^3 U_s\sigma$ respectively. These values are smaller by a factor of 2 than the diffusivities obtained from the simulations, which incorporate hydrodynamic interactions. This suggests that the hydrodynamic reflections from the surrounding fibres enhance the sphere diffusivity.

6. Simulations with frictional contacts

In the simulations discussed so far, the contacts were assumed to be frictionless. The contact force was normal to the plane of the fibres so that there was no resistance to one fibre sliding over the other. In practice there will be some friction resisting sliding that would be expected to increase the drag on the sphere. In their experiments Milliken *et al.* found a sharp transition in the variation in drag coefficient with nL^3 from a linear dependence on nL^3 for $nL^3 < 50$ to strongly nonlinear dependence (approximately cubic) for $nL^3 > 50$. Although our simulations do show a nonlinear behaviour at high nL^3, the rate of increase is not as steep as seen in experiment. This discrepancy may be due in part to the absence of friction in the simulations.

To assess the importance of friction on the dynamics of the suspension, we performed some simulations with a simple Coulomb friction law (Moore 1975) where

the magnitude of the friction force, $\boldsymbol{F}$, is specified by

$$|\boldsymbol{F}| \begin{cases} \leqslant \chi_s |\boldsymbol{N}| & \text{fixed} \\ = \chi_d |\boldsymbol{N}| & \text{sliding.} \end{cases} \tag{6.1}$$

Here $\boldsymbol{N}$ is the normal reaction force, and χ_s and χ_d are respectively the static and dynamic coefficients of friction. The contact remains at a fixed point relative to the fibres provided that the magnitude of the force required to maintain this does not exceed the limiting value $\chi_s |\boldsymbol{N}|$. Once the fibres begin to slide there is a force of magnitude $-\chi_d |\boldsymbol{N}|$ in the direction of relative motion. Although in practice χ_s is usually slightly greater than χ_d, for simplicity we chose $\chi_s = \chi_d$ so that there is no hysteresis between sticking and sliding. As we have no detailed information on the friction coefficient between the fibres used in the experiment a value of 0.4 was chosen for χ_s as being a typical coefficient for polymeric materials.

For a fixed contact, we replace the normal reaction force $\boldsymbol{N}_k$ (whose direction is perpendicular to the fibres) with a general contact force $\boldsymbol{F}_k$ of unknown direction, with equation (2.4) replaced by

$$\dot{\boldsymbol{x}}_\alpha - \dot{\boldsymbol{x}}_\beta + \lambda_\alpha^k \dot{\boldsymbol{p}}_\alpha - \lambda_\beta^k \dot{\boldsymbol{p}}_\beta = 0. \tag{6.2}$$

To be consistent, the friction law requires that the ratio of the tangential to normal components of $\boldsymbol{F}_k$ should not exceed χ_s,

$$\frac{|\boldsymbol{F}_k \wedge (\boldsymbol{p}_\alpha \wedge \boldsymbol{p}_\beta)|}{\boldsymbol{F}_k \cdot (\boldsymbol{p}_\alpha \wedge \boldsymbol{p}_\beta)} \leqslant \chi_s \tag{6.3}$$

as otherwise the contact must slip.

To treat a sliding contact we retain the normal reaction force $\boldsymbol{N}_k$, but introduce an additional friction force

$$\boldsymbol{R}_k = -\chi_d |\boldsymbol{N}_k| \hat{\boldsymbol{u}}_c, \tag{6.4}$$

where $\hat{\boldsymbol{u}}_c$ is the unit vector parallel to the relative velocity of the contact point in the absence of this force

$$\boldsymbol{u}_c = \dot{\boldsymbol{x}}_\alpha - \dot{\boldsymbol{x}}_\beta + \lambda_\alpha^k \dot{\boldsymbol{p}}_\alpha - \lambda_\beta^k \dot{\boldsymbol{p}}_\beta.$$

The friction force does not induce any relative motion perpendicular to $\boldsymbol{u}_c$. The condition for sliding motion to be present is that the contact point must move in the same direction as $\hat{\boldsymbol{u}}_c$ when the friction force is included. If the friction force reverses the direction of motion then it is too strong and the contact should be of fixed type. Friction between the sphere and a contacting fibre is treated in a similar manner.

One difficulty associated with implementing this form of friction law numerically is the changing nature of the friction force. When the contact point is fixed the friction acts as a constraint force, whereas in a sliding contact the friction force is determined by the magnitude of the normal reaction force. However, we do not know *a priori* whether a particular contact will be fixed or sliding. We determine the type of each contact, *sliding* or *fixed* via an iterative scheme. At each timestep we begin by assuming that all contacts are fixed and solve for the forces. (Although it might be thought that using the state of the contact at the previous timestep would be a better starting point, we found in practice that starting with all the contacts as fixed gave better convergence.) Those contacts that violate the static friction law are then set to sliding and all the forces recalculated. In each subsequent iteration we check the validity of the friction law at each contact and switch the status of those that violate it, until we reach a state where all the contacts are valid. By choosing χ_s equal to χ_d
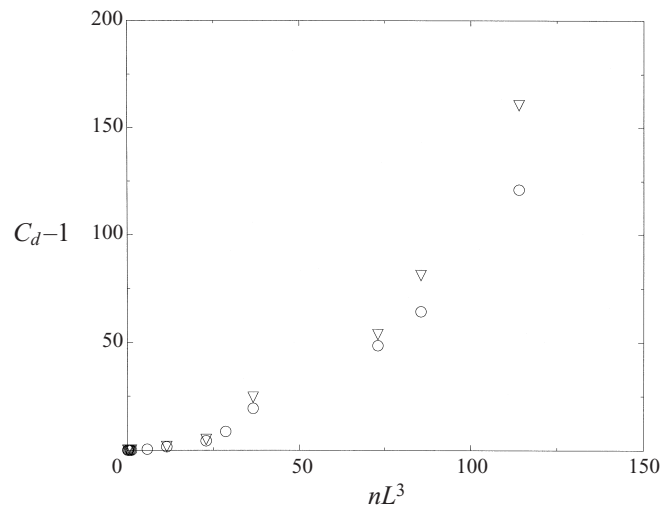
FIGURE 14. Plot showing the effect of including friction on the drag coefficient on the sphere:
○, simulations without friction ($\chi_s = \chi_d = 0$); ▽, simulations with $\chi_s = \chi_d = 0.4$.

this state is unique. Typically four iterations are required, while all cases converged within at most nine iterations.

At dilute concentrations, $nL^3 < 1$, including friction has a negligible effect on the drag coefficient. For simulations without hydrodynamic interactions the best fit to the dilute asymptote is $C_d = 1 + 0.077nL^3$ compared to $C_d = 1 + 0.073nL^3$ for frictionless contacts. Friction only becomes significant at higher concentrations where there are clusters of fibres in contact with one another. Friction restricts the ability of the clusters to deform and disperse and so increases the resistance on the sphere. The drag coefficients for simulations with and without friction are compared in figure 14. All these results are for simulations without hydrodynamic interactions. As might be expected, at high fibre concentrations friction increases the rate at which the drag increases with nL^3, so that at the highest concentration, $nL^3 = 120$, the drag is larger by roughly a factor of 4/3 in the simulations with friction. However, despite this increase in the nonlinearity of the drag coefficient with nL^3, the nonlinearity is still somewhat weaker than that observed in the experiments.

7. Simulations of a monolayer of fibres

In order to gain insight into the effect of large numbers of collisions, we performed some simulations of a monolayer of fibres, where the positions and orientation of the fibres are confined to a plane. In a semi-concentrated three-dimensional fibre suspension with $1/L^2d \ll n \ll 1/Ld^2$, the finite aspect ratio leads to two effects: a fibre cannot rotate (even in a linear flow) without colliding with its neighbours; and excluded volume effects may lead to a preferred fibre orientation. Similar phenomena occur in a monolayer with $1/L^2 \ll n \ll 1/Ld$. Simulation of a two-dimensional semi-concentrated suspension is much more tractable than a three-dimensional semi-concentrated suspension that would need to include many more fibres and also resolve the effects of finite (but large) aspect ratio on the mechanical contacts between fibres.

In the monolayer the positions and orientations of the particles are confined to lie in a plane, but their mobilities and hydrodynamic interactions are the same as for
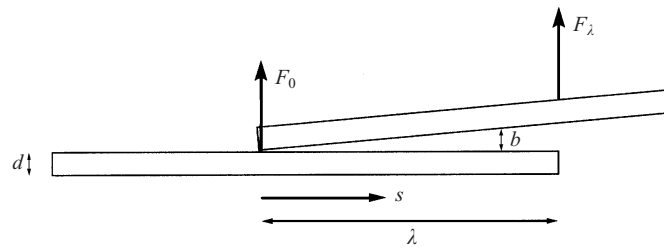
FIGURE 15. Sketch showing the definition of forces and distances in the lubrication analysis of two nearly aligned fibres.

a three-dimensional fluid. In this respect we imagine the monolayer is held between two semi-infinite domains of the fluid. It is important to distinguish this system from a two-dimensional system of lines and circles undergoing a two-dimensional flow. The two-dimensional system corresponds to a suspension of slabs that are infinitely long in the neutral direction. The hydrodynamic interactions in such a system are very strong as noted in a study of extensional viscosity by Sundarajakumar, Koch & Shaqfeh (1994).

There are a number of important differences between contacts in the monolayer and the semi-dilute suspensions described earlier. In particular, contacts are now formed between the end of one fibre and the side of another, whereas in semi-dilute suspensions the contacts are side-to-side. The reaction force now acts within the plane of the suspension in the direction perpendicular to the side contacted fibre. The procedure for checking for new contacts is slightly different to that outlined in §2. In two dimensions, two non-parallel lines will always intersect, so that step two is unnecessary. The contact first occurs when the intersection point is a distance $L/2$ from the centre of one fibre and less than $L/2$ from the centre of the other.

7.1. *Lubrication force between fibres*

Another important difference is that we now find significant numbers of close interactions between almost parallel fibres. In a semi-dilute suspension contacts between parallel fibres are very rare and can be neglected; however this is not true for a mono-layer of fibres or a semi-concentrated suspension as contact between fibres causes them to align. Unlike the case of non-parallel fibres where lubrication forces may be neglected (see §2), when contact occurs along a significant fraction of the length of the fibres the lubrication force is large and must be included. An important difference between lubrication and contact forces is that whereas contact forces are single signed, lubrication forces resist separation as well as interpenetration of the fibres.

The lubrication force between two fibres becomes important when two fibres that are already in contact at one point, become aligned such that the separation between the fibres is small compared to the fibre diameter d over a distance, λ, of the order of the fibre length L (see figure 15). The relative motion of the two fibres can be split into a sliding motion parallel to the fibre axes and a squeezing motion that corresponds to a relative rotation about the contact point. If we define a coordinate s as distance from the contact point, then the gap between the fibres at s is given by

$$b(s) = \frac{\epsilon ds}{2\lambda},$$

where $\epsilon d/2$ is the gap width at λ. Using standard lubrication theory we find that the

force densities at s parallel and perpendicular to the fibre are given respectively by

$$f_\parallel(s) = \mu\pi\dot\lambda \left(\frac{d}{2b}\right)^{1/2}, \quad f_\perp(s) = \frac{3\mu\pi}{2}\dot{b}\left(\frac{d}{2b}\right)^{3/2}. \tag{7.1}$$

For numerical convenience we replace these force distributions by two point forces at $s = 0$ and $s = \lambda$ of magnitudes F_0 and F_λ respectively, directed perpendicular to the fibre and a 'friction' $F_\parallel$ parallel to the fibre axis. F_0 can be absorbed into the contact force at $s = 0$ and so we introduce a new contact force F_λ at $s = \lambda$ that prevents relative perpendicular motion of the fibres on the lengthscale of the fibre. The magnitude of F_λ can be related to the change in ϵ from the net torque about $s = 0$. This gives

$$F_\lambda = \frac{\mu\pi\lambda^2 d}{2}\epsilon^{-3/2}\frac{d\epsilon}{dt}$$

so that the dimensionless gap width ϵ evolves according to

$$\mu\pi d\epsilon^{-1/2} = \mu\pi d\epsilon_0^{-1/2} - \int \frac{F_\lambda(t)}{\lambda}dt, \tag{7.2}$$

where ϵ_0 is the dimensionless gap width at which the lubrication force is introduced. Unlike other contacts the forces in a lubricating contact may be negative, but the lubrication contact is deemed to have broken once $\epsilon > \epsilon_0$.

The friction force $F_\parallel$ is found to be

$$F_\parallel = -2\mu\pi\epsilon^{-1/2}\lambda\frac{d\lambda}{dt} \tag{7.3}$$

from which the tangential motion may be calculated.

Strictly these approximation are only valid for $\epsilon \ll 1$; however, because of the difficulty in resolving very small angles numerically it is necessary to introduce lubrication forces when ϵ is greater than unity. The results are however found to be fairly insensitive to ϵ_0, with a ten-fold variation in ϵ giving only a 5% change in the additional drag.

Lubrication also affects the mobility of the fibres. A pair of fibres in lubricating contact will behave as a single fibre of length $2L - \lambda$, as they are held together by lubrication forces. Consequently, each fibre has in effect half the translational and orientational hydrodynamic resistance of the compound fibre of length $2L - \lambda$. More generally, each fibre in a bundle of k fibres held together by lubrication forces will have an effective hydrodynamic resistivity equal to $1/k$th of that of the corresponding compound fibre.

7.2. *Initial orientation distribution*

A semi-concentrated suspension of Brownian fibres undergoes an order transition from a isotropic phase (for $nL^2 d < 4.19$) to nematic liquid crystal (for $nL^2 d > 5.33$) with a mixture of the two phases at intermediate concentrations (Lekkerkerker *et al.* 1984). However, in their Monte-Carlo simulations Frenkel & Eppenga (1985) found that a two-dimensional suspension of Brownian hard lines never forms a true liquid crystal. Instead there is a transition from an isotropic phase for $nL^2 < 7$ to a phase with 'pseudo-long-range' order for $nL^2 > 7.5$, where the correlation between fibre orientations decays algebraically over distance large compared to the fibre length.

Due to the high computational cost of using Monte-Carlo simulations of this kind to determine an initial fibre distribution, we chose to use the much simpler technique
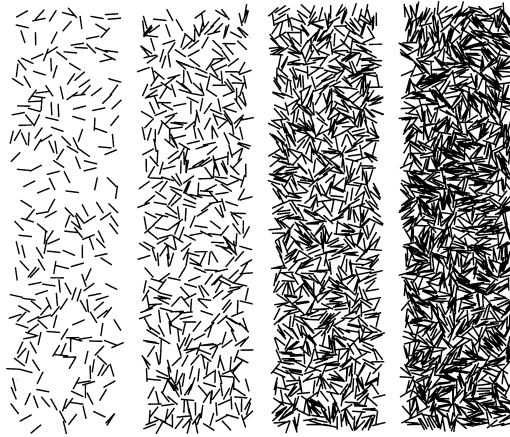
FIGURE 16. Examples of initial configurations of monolayers of fibres at $nL^2 = 1, 2, 4$ and 6.

of placing each fibre down at random in turn disgarding any placement in which fibres intersect. For fibre concentrations up to nL^2 of 6, there was no significant difference between the order parameters of distributions produced in this way and those found by Frenkel & Eppenga. In any case mixing the fibres by other methods, such as by a mechanical stirrer, will not necessarily produce the same distribution as Brownian mixing. Examples of the initial orientation distributions of the fibres are shown in figure 16.

7.3. *Drag coefficient on the sphere*

The simulations were run in the same manner as the three-dimensional calculations described earlier. The sphere was released above a column of suspended fibres, and the drag coefficient determined from the time-of-flight. In view of the large number of short-range interactions we did not include the long-range multiparticle interactions in these simulations, although the effects of the short-range lubrication forces were included.

Figure 17 shows a series of snapshots of the suspension during the early phase of the sphere descent. As there are no long-range hydrodynamic interactions, the fibres only move when they are struck by the sphere or another fibre. At any moment in time the sphere is in one of three modes, 'free-fall', 'rolling' or 'blockage clearing'.

In the free-fall mode the sphere is not in contact with any fibres and falls vertically until it hits the first fibre blocking its path (figure 17*a*). In the rolling phase, the sphere moves by rolling along the surface of a fibre (figure 17*b*). The contact force between the sphere and the fibre causes the fibre to rotate. The sphere will continue to roll down the fibre until it either rolls off the end or strikes another fibre which blocks its motion (as is about to happen in figure 17*b*). In order to make further progress the sphere must clear the blockage by pushing the fibres aside sufficiently to produce a gap large enough for it to move through. Examples of this can been seen from figure (17*c, d*). Clearing these blockages is the major cause of delay in the sphere's motion through the suspension.

As with the three-dimensional calculations presented earlier, the initial phase of the sphere descent is atypical, and so we disregard the motion of the sphere in the first $10L$ and final $5L$ of the column and calculate the drag coefficient from the time required to fall through the remainder of the column. The results for different fibre
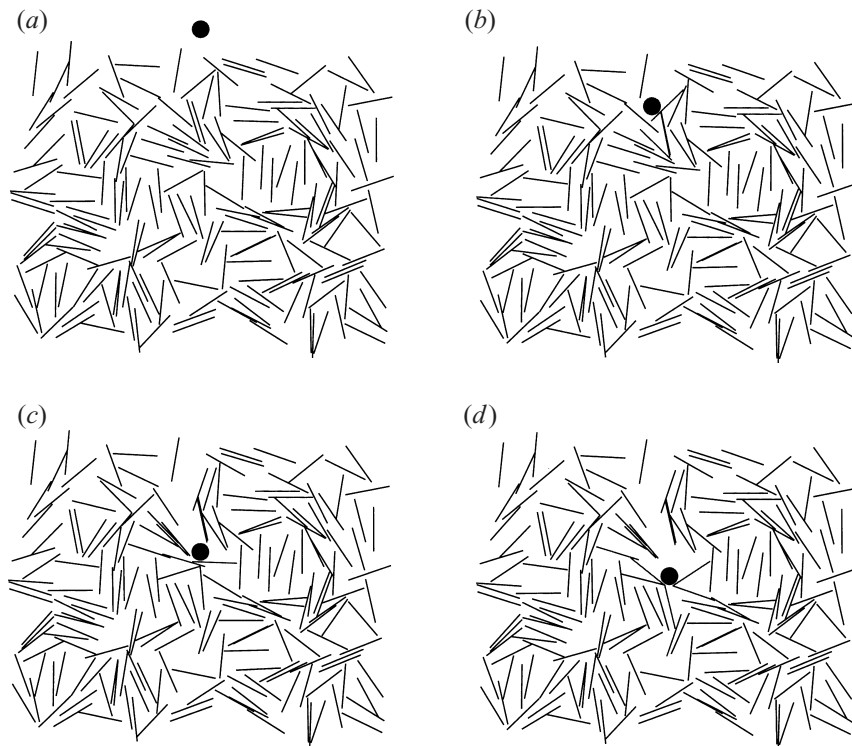
FIGURE 17. Snapshots of the motion of a sphere of diameter $0.4L$ falling through a monolayer of density $nL^2 = 4$, showing the three modes of motion. In (*a*) the sphere is in 'free-fall', while in (*b*) it descends by 'rolling' along a fibre. In (*c*) and (*d*) the motion is 'blocked' by two or fibres, that must be cleared out of the way before the sphere can continue to descend.

concentrations are plotted in figure 18 up to $nL^2 = 6$ with error bars representing the standard error on the mean. It can be seen that the drag coefficient increases linearly with nL^2 as $C_d \simeq 1 + 0.25nL^2$.

It is remarkable that the dependence of the drag on the concentration remains linear up to concentrations almost as high as the transition to pseudo-long-range order. We would expect to see a nonlinear increase in drag once nL^2 exceeded unity, similar to that observed in §3 for a semi-dilute suspension. In the mono-layer, the addition to the drag coefficient caused by the fibres comes mainly from clearing blockages. The number of blockages should be proportional to the number density of fibres, suggesting that the time required to clear a blockage is roughly independent of the fibre concentration.

The variation in the drag coefficient at $nL^2 = 2$ with sphere size is shown in figure 19, for sphere diameters ranging from $0.2L$ to $0.8L$. In contrast to the three-dimensional calculations where there was significant variation in the drag coefficient with sphere diameter, the drag coefficient for the monolayer is found to be independent of sphere size. At moderate to large values of nL^2, the explanation for this result comes from the observation that the additional drag caused by the fibres is predominantly from clearing blockages. The rate at which a blockage can be cleared is proportional to the force applied by the sphere from its weight. In our non-dimensionalization this rate is proportional to the sphere diameter, σ, so that the time per blockage scales as $1/\sigma$. However the number of gaps that are too small for the sphere to pass through scales
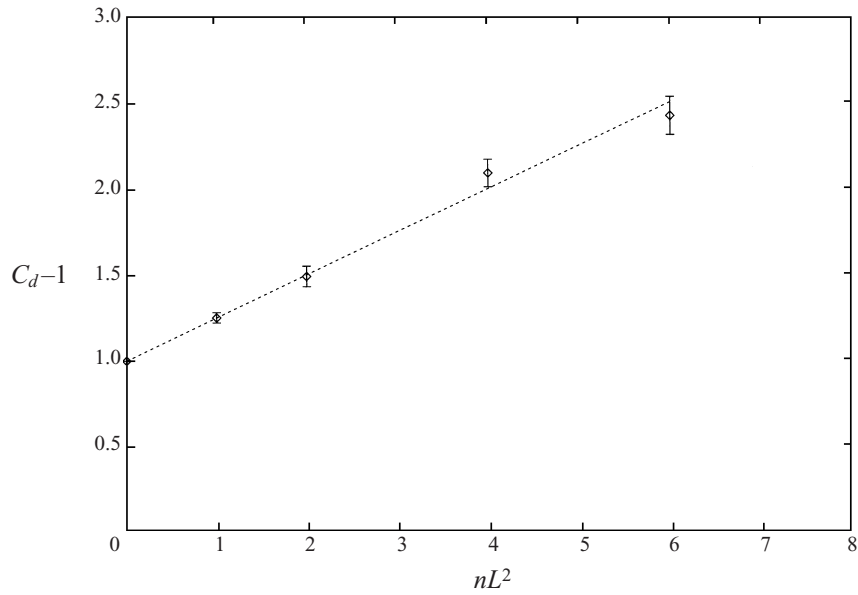
FIGURE 18. Drag coefficient, C_d, as a function of nL^2 for a monolayer of fibres and sphere of diameter $0.4L$. The error bars indicate the standard error on the mean and the dotted line indicates $C_d = 1 + 0.25nL^2$.
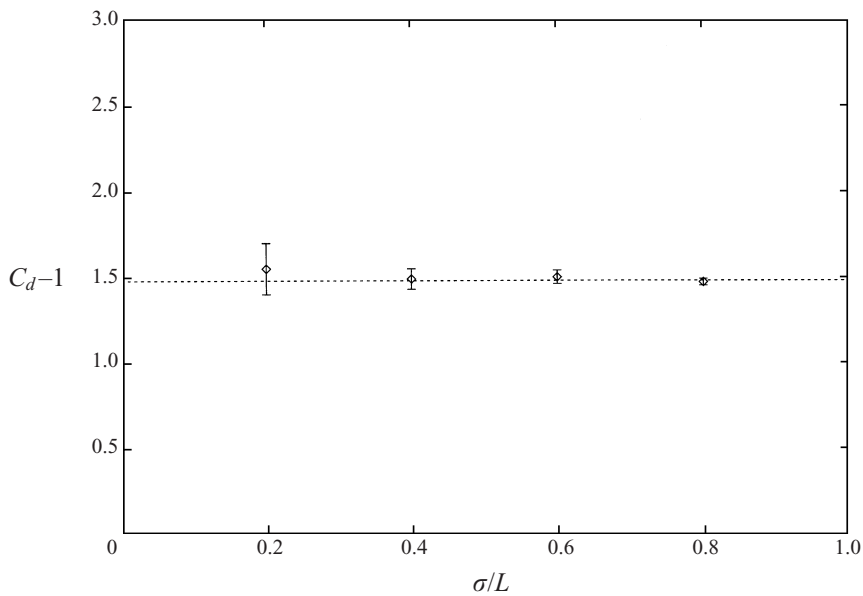
FIGURE 19. Drag coefficient, C_d, as a function of sphere diameter σ/L for a monolayer of fibres of density $nL^2 = 2$. The error bars indicate the standard error on the mean.

with σ so that the product of the number of blocks with the time delay per block is independent of σ. As the number of blocks in any particular run is proportional to σ the magnitude of the variation in drag coefficients between runs should be inversely proportional to σ as can be seen from the magnitude of the error bars in figure 19.

In the limit of small σ/L and nL^2 it can be shown that the drag should vary weakly with the logarithm of σ/L. In this limit we assume that the sphere does not disturb the fibre, but rolls along its length until it reaches the end. If we attempt the analysis done in §4.2 for the monolayer, we find that the additional time, $\sum \Delta T_i$ required to fall through a depth, H, is given by

$$\frac{U_0}{H} \sum \Delta T_i = \frac{nL^2}{\pi} \int_0^{\pi/2} \tan\theta \, \mathrm{d}\theta \qquad (7.4)$$

which has a logarithmic divergence at $\theta = \pi/2$. For fibres close to the horizontal the time required for an infinitesimally small sphere to roll off the fibre diverges as $1/(\pi/2 - \theta)$. For finite values of σ/L the rotation of the fibre by the sphere will remove the divergence for angles where $\pi/2 - \theta \sim \sigma/L$. Consequently

$$C_d \sim 1 + \frac{nL^2}{\pi} \log\left(\frac{L}{\sigma}\right). \qquad (7.5)$$

An over-riding concern with all these results is to what extent they can be carried over to three-dimensional semi-concentrated suspensions. Qualitatively at least we would expect the problem of clearing blockages caused by a number of intersecting fibres to appear in three-dimensional suspensions at sufficiently high concentrations. However the scalings may be quite different.

Our results are restricted to concentrations within the isotropic regime. In order to consider higher concentrations we would require a column of fibres large compared to the persistence length of the orientation distribution and not just the fibre length so that the sphere encounters the full spectrum of local orientations. Given the rather special nature of planar suspensions in having states of algebraic orientational order, we did not pursue this.

8. Conclusions

The simulation technique described in this paper differs from those used by previous workers in studying spheres and moderate-aspect-ratio particles, in that we explicitly include contact forces between the particles. The lubrication force between high-aspect-ratio particles is so weak that even particles with atomic-scale roughness will come into mechanical contact. The presence of these non-hydrodynamic forces means that such suspensions do not obey Stokes flow reversibility. Lubrication forces only become important when fibres are nearly aligned, and are of significance only in semi-concentrated suspensions.

The main purpose of this paper is to demonstrate the importance of fibre–fibre contact forces on the flow properties of suspensions of non-Brownian fibres. As noted in the introduction, much of the recent work on fibre suspensions has focused on calculating the effects of the long-range hydrodynamic interactions, on the basis that these are the dominant interactions at low concentrations. While this is true for linear flows, where fibre–fibre contacts are negligible for $nL^2d \ll 1$, it does not hold for flows that are nonlinear on the length scale of the fibres. In §3 we showed that even the linear dependence of the drag on a sphere with nL^3 in the limit of low concentrations is affected by fibre–fibre contacts. In this flow hydrodynamic interactions and fibre–fibre contacts are of equal importance at low and moderate values of nL^3, and only by including both effects are we able to obtain quantitative agreement with the experiments of Milliken et al.

We would expect fibre–fibre contacts to be of equal importance in other nonlinear flows, for example flows through narrow channels or around small obstacles that occur in injection moulding. In another study using the same method of simulation, Sundararajakumar & Koch (1997) show that in shear-flow fibre–fibre contacts produce a dramatic rise in viscosity for nL^2d of order unity.

Our results also call into question the interpretation of the drag coefficient on a small sedimenting sphere as a measure of fluid viscosity. The drag coefficient was found to vary with the ratio of sphere diameter to fibre length, with a maximum drag coefficient for spheres of diameter roughly equal to the length of the fibres. However, the drag coefficient may be regarded as giving a measure of the resistance to flows with a characteristic lengthscale equal to the sphere diameter. Thus the falling ball provides a convenient probe of mechanical contacts that may arise in many nonlinear flows.

REFERENCES

ABBOTT, J. M., GRAHAM, A. L., MONDY, L. A. & BRENNER, H. 1998 Dispersion of a ball settling through a quiescent neutrally buoyant suspension. *J. Fluid Mech.* **361**, 309–331.

BATCHELOR, G. K. 1970 Slender-body theory for particles of arbitrary cross-section in Stokes flow. *J. Fluid Mech.* **44**, 419–440

BATCHELOR, G. K. 1971 The stress generated in a non-dilute suspension of elongated particles by pure straining motion. *J. Fluid Mech.* **46**, 813–829.

BIBBO, M. A. 1987 Rheology of semiconcentrated fibre suspensions. PhD thesis, MIT.

BRADY, J. F. & BOSSIS, G. 1988 Stokesian dynamics. *Ann. Rev. Fluid Mech.* **20**, 111–157.

CATES, M. E. & EDWARDS, S. F. 1984 Linear-theory of disordered fibre-reinforced composites. *Proc. R. Soc. Lond.* A **395**, 89–109.

CHWANG, A. T. & WU, T. Y. 1975 Hydrodynamics of low-Reynolds-number flow. Part 2. Singularity methods for Stokes flows, *J. Fluid Mech.* **67**, 787–815.

CLAEYS, I. L. & BRADY, J. F. 1993a Suspensions of prolate spheroids in Stokes flow. Part 1. Dynamics of a finite number of particles in an unbounded flow. *J. Fluid Mech.* **251**, 411–442.

CLAEYS, I. L. & BRADY, J. F. 1993b Suspensions of prolate spheroids in Stokes flow. Part 2. Statiscally homogeneous dispersions. *J. Fluid Mech.* **251**, 443–477.

DOI, M. & EDWARDS, S. F. 1986 *The Theory of Polymer Dynamics.* Clarendon.

FREDRICKSON, G. H. & SHAQFEH, E. S. G. 1989 Heat and mass-transport in composites of aligned slender fibres. *Phys. Fluids* A **1**, 3–20.

FRENKEL, D. & EPPENGA, R. 1985 Evidence for algebraic orientational order in a two-dimensional hard-core nematic. *Phys. Rev.* A **31**, 1776–1787.

FRENKEL, D. & MAGUIRE, J. F. 1983 Molecular dynamics study of the dynamical properties of an assembly of infinitely thin hard rods. *Mol. Phys.* **49**, 503–541.

KOCH, D. L. & SHAQFEH, E. S. G. 1990 The average rotation rate of a fibre in the linear flow of a semidulate suspension. *Phys. Fluids* A **2**, 2093–2102.

LADD, A. J. C. 1989 Hydrodynamic interactions and the viscosity of suspensions of freely moving spheres. *J. Chem. Phys.* **90**, 1149–1157.

LEKKERKERKER, H. W. W., COULON, P., VAN DER HAEGEN, R. & DEBLIECK, R. 1984 On the isotropic-liquid crystal phase-separation for solutions of rodlike particles of different lengths. *J. Chem. Phys.* **80**, 3427–3433.

MACKAPLOW, M. B. & SHAQFEH, E. S. G. 1996 A numerical study pf the rheological properties of suspensions of rigid, non-Brownian fibres. *J. Fluid Mech.* **329**, 155–186.

MILLIKEN, W. J., GOTTLIEB, M., GRAHAM, A. L., MONDY, L. A. & POWELL, R. L. 1989 The viscosity volume fraction relation for suspensions of rod-like particles by falling ball rheometry. *J. Fluid Mech.* **202**, 217–232.

MONDY, L. A., INGER, M. S. & DINGMAN, S. E. 1991 Boundary element method simulations of a ball falling through quiescent suspensions. *J. Rheol.* **35**, 825–848.

MONDY, L. A., MORRISON, T. G., GRAHAM, A. L. & POWELL, R. L. 1990 Measurements of the viscosities of suspensions of oriented rods using falling ball rheometry. *Intl J. Multiphase Flow* **16**, 651–662.

MOORE, D. F. 1975 *Principles and Applications of Tribology.* Pergamon.

POWELL, R. L., MORRISON, T. G. & MILLIKEN, W. J. 1998 Rheology of suspensions of rods using falling ball rheometry. *Phys. Fluids* (submitted).

RAHNAMA, M., KOCH, D. L. & SHAQFEH, E. S. G. 1994 The effect of hydrodynamic interactions on the orientation distribution in a fibre suspension subject to simple shear flow. *Phys. Fluids* **7**, 487–506.

RALAMBOTIANA, T., BLANC, R. & CHAOUCHE, M. 1997 Viscosity scaling in suspensions of non-Brownian rodlike particles *Phys. Fluids.* **9**, 3588–3594.

ROSENBERG, J., DENN, M. & KEUNINGS, R. 1990 Simulations of non-recirculating flows of dilute fibre suspensions. *J. Non-Newtonian Fluid Mech.* **37**, 317–245.

RUSSEL, W. B., HINCH, E. J., LEAL, L. G. & TIEFFENBRUCK, G. 1971 Rods falling near a vertical wall. *J. Fluid Mech.* **83**, 273.

SANDSTROM, C. R. & TUCKER, C. L. 1993 A theory for concentrated fibre suspension with strong fibre-fibre interactions. *Makromolekulare Chemie – Macromolecular Symposia* **68**, 291–300.

SANGANI, A. S. & MO, G. B. 1996 An O(N) algorithm for Stokes and Laplace interactions of particles. *Phys. Fluids* **8**, 1990–2010.

SHAMES, I. H. 1979 *Mechanics of Deformable Bodies.* Robert E. Krieger Publishing Co. Huntington, New York.

SHAQFEH, E. S. G. 1988 A nonlocal theory for the heat-transport in composites containing highly conducting fibrous inclusions. *Phys. Fluids* **31**, 2405–2425.

SHAQFEH, E. S. G. & FREDRICKSON, G. H. 1990 The hydrodynamic stress in a suspension of rods. *Phys. Fluids* A **2**, 7–24.

STOVER, C. A. & COHEN, C. 1990 The motion of rodlike particles in the pressure driven flow between two flat plates. *Rheol. Acta* **29**, 192–203.

SUNDARARAJAKUMAR, R. R. & KOCH, D. L. 1997 Structure and properties of sheared fibre suspensions with mechanical contacts. *J. Non-Newtonian Fluid Mech.* **73**, 205–239.

SUNDARARAJAKUMAR, R. R., KOCH, D. L. & SHAQFEH, E. S. G. 1994 The extensional viscosity and effective thermal conductivity of a dispersion of aligned disks. *Phys. Fluids* **6**, 1955–1962.

TOLL, S. F. & MANSON, J.-A. E. 1994 Dynamics of a planar concentrated fibre suspension with non-Hydrodynamic interaction. *J. Rheol.* **38**, 985–997.

YUAN, X. F. & BALL, R. C. 1994 Rheology of hydrodynamically interacting concentrated hard disks. *J. Chem. Phys.* **101**, 9016–9021.